UNIVERSITY OF LEEDS

This is a repository copy of *Zn stable isotope fractionation during adsorption onto todorokite: A molecular perspective from X-ray absorption spectroscopy and density functional theory*.

White Rose Research Online URL for this paper:
https://eprints.whiterose.ac.uk/187500/

Version: Accepted Version

Article:
Wang, Z, Kwon, KD, Peacock, C orcid.org/0000-0003-3754-9294 et al. (4 more authors) (2022) Zn stable isotope fractionation during adsorption onto todorokite: A molecular perspective from X-ray absorption spectroscopy and density functional theory. Geochimica et Cosmochimica Acta, 327. pp. 116-136. ISSN 0016-7037

https://doi.org/10.1016/j.gca.2022.04.016

© 2022, Elsevier. This manuscript version is made available under the CC-BY-NC-ND 4.0 license http://creativecommons.org/licenses/by-nc-nd/4.0/.

Reuse
This article is distributed under the terms of the Creative Commons Attribution-NonCommercial-NoDerivs (CC BY-NC-ND) licence. This licence only allows you to download this work and share it with others as long as you credit the authors, but you can’t change the article in any way or use it commercially. More information and the full terms of the licence here: https://creativecommons.org/licenses/

Takedown
If you consider content in White Rose Research Online to be in breach of UK law, please notify us by emailing eprints@whiterose.ac.uk including the URL of the record and the reason for the withdrawal request.

White Rose university consortium
Universities of Leeds, Sheffield & York

eprints@whiterose.ac.uk
https://eprints.whiterose.ac.uk/

Prepared for *Geochim. Cosmochim. Acta*

Zn stable isotope fractionation during adsorption onto todorokite: A molecular perspective from X-ray absorption spectroscopy and density functional theory

Zhao Wang[a,f], Kideok D. Kwon[b], Caroline Peacock[c], Xinxin Mo[a,d,f], Wenxian Gou[a,f], Xionghan Feng[e], Wei Li[a,f,*]

[a] Key Laboratory of Surficial Geochemistry, Ministry of Education, School of Earth Sciences and Engineering, Nanjing University, Nanjing 210023, China

[b] Department of Geology, Kangwon National University, Chuncheon 24347, Republic of Korea

[c] School of Earth and Environment, University of Leeds, Leeds, LS2 9JT, UK

[d] Department of Earth and Planetary Science, Graduate School of Science, The University of Tokyo, Hongo 7-3-1, Bunkyo-ku, Tokyo 113-0033, Japan

[e] State Environmental Protection Key Laboratory of Soil Health and Green Remediation, College of Resources and Environment, Huazhong Agricultural University, Wuhan 430070, China

[f] Frontiers Science Center for Critical Earth Material Cycling (FSC-CEMaC), Nanjing University, Nanjing, 210023, China

* Corresponding author, Tel: +0086-25-89681539; Fax: +0086-25-83686016; Email: liwei_isg@nju.edu.cn

Abstract

Mineral-solution interface reactions control the mobility and fate of trace metals (e.g., Zn) and may drive their associated isotopic fractionation in the natural environment, but understanding the coupling between interfacial reactions and isotopic behavior requires a molecular-level understanding of these processes. In this study, we investigate Zn stable isotope fractionation during adsorption to todorokite as a function of reaction time, pH and Zn concentrations. We show that Zn stable isotope fractionation reaches equilibrium at ~12 h reaction time at pH 6 and Zn concentrations of 0.05 mM. For Zn concentrations of 0.05 and 0.2 mM, Zn isotopic fractionation between adsorbed and aqueous Zn ($\Delta^{66}Zn_{adsorbed\text{-}aqueous}$) is approximately −0.1 ± 0.04‰ at pH 3−5, and $\Delta^{66}Zn_{adsorbed\text{-}aqueous}$ gradually increases from −0.1 ± 0.04‰ to 0.05 ± 0.05‰ at higher pH 6-8. Extended X-ray absorption fine structure (EXAFS) spectroscopy shows that Zn adsorbs to the todorokite surface as an outer-sphere octahedral complex with an average Zn−O interatomic distance of 2.06 Å at pH 3. In contrast, Zn is predominantly present as a tetrahedral coordinated structure with a shorter average Zn−O interatomic distance of ~2.00−2.05 Å at pH 6 and 8, suggesting the presence of a mixture of octahedral outer-sphere and tetrahedral inner-sphere surface complexes. Density functional theory calculations suggest that outer-sphere surface complexes exist in the center of the structural tunnels of todorokite, yielding a theoretical Zn isotopic fractionation ($\Delta^{66}Zn_{adsorbed\text{-}aqueous}$) of −0.2‰ to −0.3‰, whereas the tetrahedral inner-sphere surface complex results in a large $\Delta^{66}Zn_{adsorbed\text{-}aqueous}$ of +0.5‰ to +0.8‰. Combined laboratory experiments and theoretical calculations demonstrate that different magnitudes of Zn isotopic fractionation are controlled by structural changes (e.g., coordination and bond distance) in the Zn surface complexes formed on todorokite relative to its aqueous form (i.e., aqua $Zn(H_2O)_6^{2+}$). These results provide important new constraints for understanding Zn isotope signatures in natural Mn-rich sediments and lead to a more complete understanding of Zn isotopes in the ocean.

Keywords: Mn oxide; zinc; adsorption; sorption; stable isotope; fractionation; surface precipitation; EXAFS; DFT

1. Introduction

Metals such as zinc (Zn) play a dual role in the Earth system. On the one hand, they are important micronutrients required by organisms for their life processes (Sinoir et al., 2012; Moore et al., 2013). In the oceans, for example, metals support photosynthesis and thus the drawdown of carbon dioxide, so their concentrations in seawater are critical for regulating climate (Morel et al., 1994). On the other hand, at elevated concentrations, these same metals are toxic, and their release through human activities causes severe pollution (Sandstead, 2014). Studying the biogeochemical cycling of metals and how these cycles control metal concentrations is therefore critically important to understand the role and fate of metals in the Earth system.

Excitingly stable metal isotopes provide an original perspective for tracking metal cycling because stable metal isotope signatures can be used as a "fingerprint" to pinpoint specific metal sources and processes that control metal mobility and fate (Wiederhold, 2015). In particular, Zn isotopes have the potential to shed light on the oceanic biogeochemical cycling of Zn (Conway and John, 2014; Little et al., 2014; Conway and John, 2015; John et al., 2014; Little et al., 2016; Vance et al., 2016; Sweere et al., 2018). In the Zn oceanic cycle, the Zn isotopic composition of the dissolved pool (~0.5‰ in $\delta^{66}Zn_{JMC}$) is substantially heavier than the best estimates of the Zn isotopic composition of the input fluxes to the ocean (≤ 0.3‰ in $\delta^{66}Zn_{JMC}$), such as rivers, dust, hydrothermal fluids and benthic fluxes (Conway and John, 2014; Little et al., 2014; Little et al., 2016; Liu et al., 2019). Marine oxic sediments (e.g., manganese oxides and carbonates) scavenge isotopically heavy Zn (~0.9‰ in $\delta^{66}Zn$) (Pichat et al., 2003; Little et al., 2014; Bryan et al., 2015; Dong et al., 2016), but organic-rich continental margin sediments bury light Zn (Little et al., 2016). The processes that control the mobility and fate of Zn and how these processes determine its associated isotopic behavior and isotopic composition in the oceans, however, are poorly understood (Little et al., 2016; Vance et al., 2016; Isson et al., 2018). The lack of knowledge on Zn uptake, retention and biogeochemical behavior in marine sediments and how this impacts Zn isotopic signatures means that the application of Zn isotopes to constrain Zn mass balance, required for an improved understanding of Zn cycling, is speculative. Investigating Zn uptake, retention and isotope fractionation during adsorption to marine minerals can shed light on these knowledge gaps.

Significant isotopic fractionations are observed during mineral-solution interface reactions in a variety of aqueous environments (including marine sediments and terrestrial soils, rivers, aquifers and

wetlands) (Wasylenki et al., 2014; Wiederhold, 2015; Vance et al., 2016). Detailed information on Zn isotopic fractionation during its adsorption to a variety of mineral surfaces is summarized in Table 1 (Pokrovsky et al., 2005; Balistrieri et al., 2008; Juillot et al., 2008; Bryan et al., 2015; Dong and Wasylenky, 2016; Guinoiseau et al., 2016; Nelson et al., 2017; Gou et al., 2018). The first investigation of Zn isotope fractionation during adsorption to minerals reports that heavy Zn isotopes are enriched on pyrolusite, hematite, gibbsite and corundum surfaces, while light Zn isotopes preferentially adsorb to birnessite and goethite (Pokrovsky et al., 2005). Since this study, however, Zn isotopic fractionation during adsorption to birnessite has been found to be significantly influenced by solution ionic strength and Zn surface loading (Bryan et al., 2015). At low ionic strength, there is a small kinetic effect ($\Delta^{66}Zn_{adsorbed-aqueous} \sim -0.2‰$) for experimental durations up to 48 hours, but after 100 hours, fractionations are indistinguishable from zero ($\Delta^{66}Zn_{adsorbed-aqueous} = 0.05 \pm 0.08‰$). At high ionic strength, heavy isotopes are always preferentially adsorbed, but there is a strong dependence on surface loading, with $\Delta^{66}Zn_{adsorbed-aqueous} = 2.74‰$ at low surface loadings, which is reduced to 0.16‰ for high surface loadings. In addition, an enrichment of heavy isotopes is also reported at the surface of goethite ($\Delta^{66}Zn_{adsorbed-aqueous} = 0.29 \pm 0.07‰$) (Juillot et al., 2008), which contrasts with the first reported results ($\Delta^{66}Zn_{adsorbed-aqueous} = -0.18$ to $-0.28‰$) (Pokrovsky et al., 2005). More investigations now report distinct Zn isotopic fractionation behaviors in different mineral systems (e.g., calcite, kaolinite, silicon oxides and aluminum oxide) (Dong and Wasylenky, 2016; Guinoiseau et al., 2016; Nelson et al., 2017; Gou et al., 2018). This complicated fractionation behavior means that successful application of the stable isotope fingerprinting technique to track the source and fate of Zn in the oceanic environment relies on a robust understanding of its isotopic fractionation during adsorption under different chemical conditions and to different types of mineral surfaces.

To understand Zn isotopic fractionation, it is first important to distinguish which type of fractionation dominates during interface reactions occurring in the oceanic environment. Generally, isotopic fractionations can be divided into mass-dependent (MDF) and mass-independent (MIF) fractionation, where MDF includes equilibrium fractionation, Rayleigh fractionation and kinetic fractionation (Rosman and Tatlor, 1998; Moynier et al., 2017). Zn isotopic fractionation during interface reactions has been reported to obey the MDF trend (Moynier et al., 2017). According to classical stable isotope theory, several physiochemical factors (including temperature, pressure, chemical and solution

composition, and chemical bond stiffness) should then affect this isotopic fractionation (Bigeleisen and Mayer, 1947; Schauble, 2004). For interface reactions occurring at low temperature, temperature and pressure are well constrained, and chemical composition and solution properties can be experimentally controlled and explored. This means that chemical bond stiffness should be the dominant factor controlling Zn isotopic fractionation at equilibrium. Chemical bond stiffness is directly related to the local chemical structure and thus the adsorption mechanism. Previous work with Zn (Gou et al., 2018), thallium (Peacock and Moon, 2012) and cerium (Nadaka et al., 2017) demonstrates that the application of extended X-ray absorption fine structure (EXAFS) spectroscopy can clearly determine the local chemical structure of metals associated with mineral surfaces and thus determine metal adsorption mechanisms, and these studies then relate these adsorption mechanisms to isotopic behavior to constrain the relationship between interface reactions and isotopic fractionation. In turn, this approach can be used to provide a good understanding of the origin and evolution of metal isotope signatures in the environment.

Studies reporting the application of EXAFS spectroscopy to elucidate Zn isotopic fractionation mechanisms, however, are scarce. This is due to the complexity of isotopic and EXAFS measurements and the high elemental concentration required for high-quality EXAFS spectra, which generally exceeds the workable concentration necessary for isotopic analysis. Researchers have therefore mostly measured EXAFS spectra and isotopic fractionation separately under different experimental conditions, which can lead to a mismatch between EXAFS spectra and isotopic data that obscures the relationship between adsorption mechanisms and isotopic fractionation behavior (Manceau et al., 2002; Bryan et al., 2015; Wang et al., 2018). To date, only a limited number of studies have conducted EXAFS characterization and Zn isotope measurements under the same chemical conditions (Juillot et al., 2008; Nelson et al., 2017; Gou et al., 2018). According to these studies, for Zn adsorption onto 2-line ferrihydrite, the change in $R_{Zn\text{-}O}$ values between aqueous (~2.06 Å) and adsorbed Zn (1.96 Å) explains the large isotopic fractionation ($\Delta^{66}Zn_{adsorbed-aqueous}$ = 0.53‰) (Juillot et al., 2008). In the case of goethite, no significant $R_{Zn\text{-}O}$ differences between aqueous Zn and adsorbed Zn are consistent with the small isotopic fractionation ($\Delta^{66/64}Zn_{adsorbed-aqueous}$ = 0.29‰) (Juillot et al., 2008). In the Zn-γ-Al_2O_3 system, both the $R_{Zn\text{-}O}$ and the coordination number are proposed to control isotopic fractionation (Gou et al., 2018). In silica systems, despite different coordination numbers, the isotopic fractionation factors for octahedral

and tetrahedral Zn complexes versus aqueous Zn are not distinguishable beyond uncertainties, which is attributed to the low energetic difference between octahedral and tetrahedral Zn on quartz and amorphous silica surfaces (Nelson et al., 2017). Moreover, the combined application of EXAFS spectroscopy and isotopic fractionation measurements under the same chemical conditions has not been used to constrain the relationship between interface reactions and isotopic fractionation for Zn adsorption on todorokite.

Todorokite is one of the main Mn-bearing phases in oxic marine sediments (Burns and Burns, 1977). It is commonly accepted that todorokite only forms from the transformation of birnessite precursors (Burns and Burns, 1977, Feng et al., 2004; Bodei et al., 2007; Atkins et al., 2014). Birnessite often has trace metals (e.g., Zn) adsorbed on its surface and isomorphically substituted into its structure, which can reach 10^6 times over their concentrations in seawater (Arrhenius, 1963; Koschinsky and Hein, 2003). Specifically, with regard to Zn, natural ferromanganese oxides in oxic marine sediments provide the dominant sinks for Zn in the modern marine Zn cycle (Little et al., 2013; Vance et al., 2016). These minerals typically contain between ~531$\mu g \cdot g^{-1}$ – 1845$\mu g \cdot g^{-1}$ Zn, exclusively sequestered by the Mn-rich part (Koschinsky and Halbach, 1995; Koschinsky and Hein, 2003), as a result of an adsorption equilibrium between Zn and birnessite. When todorokite forms from birnessite, however, the fate of Zn adsorbed by birnessite is likely to be ultimately controlled by its adsorption to todorokite (Atkins et al., 2016; Little et al., 2020). This interaction between Zn and todorokite thus potentially plays an important role in controlling Zn isotope compositions in seawater. Todorokite has a 3D tunnel structure consisting of triple chains of edge-sharing Mn^{4+}-O_6 octahedra that share corners, and Mn^{4+} substitution by cations of lower valence (e.g., Mn^{3+}, Ni^{2+}, Co^{3+}, or Cu^{2+}; Post, 1999; Atkins et al., 2014; Wu et al., 2019; Wegorzewski et al., 2020) creates a deficit of charge. The deficit of surface charge may be balanced by exchangeable cations, such as Tl, forming outer-sphere complexes in the todorokite tunnel structure (Wick et al., 2019) or by the formation of inner-sphere complexes on the todorokite surface. Therefore, todorokite is likely to adsorb Zn via different mechanisms and thus fractionate Zn isotopes in a variety of different ways.

In this study, we focus on the adsorption and isotopic fractionation of Zn with todorokite. Specifically, we investigate the behavior of Zn isotopes during adsorption to todorokite under various pH and Zn loading conditions and employ EXAFS spectroscopy to reveal the molecular-level

adsorption mechanism of Zn (i.e., coordination number, bond distances). Importantly, the structural information provided by EXAFS sheds light on the nature of the Zn-mineral bond stiffness that we then use to interpret the metal stable isotope fractionation signatures at equilibrium. To augment the experimental results, we also use a computational approach based on density functional theory (DFT) to simulate metal adsorption mechanisms and calculate the values of reduced partition function ratios (as 1000lnβ) for Zn bound to todorokite. Our results provide a new in-depth understanding of the coupled adsorption-fractionation behavior of Zn, which is necessary to better constrain the application of Zn isotope signatures to track the oceanic and global Zn cycle.

2. Materials and Methods

2.1. Todorokite synthesis and characterization

Todorokite was synthesized following the procedures described by Feng et al. (2004). First, 250 ml of 5.5 M NaOH solution (refrigerated for 5 h at 4 °C) was added quickly to 200 ml of 0.5 M $MnCl_2$ solution. The mixed solution was then stirred vigorously for 5 h and aerated with O_2 at a rate of 2 L min^{-1}. The resulting precipitate was washed with deionized (DI) water until the conductivity reached below 2 $\mu S \cdot cm^{-1}$. Then, the synthetic birnessite, which remained as a wet paste, was dispersed in 1 M $MgCl_2$ solution, stirred for 12 h at room temperature, and then washed three times with DI water. The resulting Mg-buserite was resuspended in a triangle flask connected to a condensation device and heated to reflux at 100 °C under stirring. After being refluxed for 24 h, the suspension was cooled to room temperature, washed until the conductivity of the supernatant reached below 2 $\mu S \cdot cm^{-1}$, and then freeze-dried for later use. The Zn impurity in synthetic todorokite was negligible, as determined by inductively coupled plasma–mass spectrometry (ICP–MS) analysis (Agilent 7700).

The synthetic todorokite was characterized using a powder X-ray diffractometer (XRD) (Bruker, D8 ADVANCE) with Cu Kα radiation (λ= 0.15418 nm). The X-ray diffractometer was operated at 40 kV and 40 mA, with a 2θ range from 5° to 60° with a step size of 0.02° and a scan speed of 1 s at each step. Similar to 10 Å phyllomanganate (i.e., Mg-buserite), todorokite has a basal d-spacing of 1 nm (Burns et al., 1983, 1985; Bodeı et al., 2007; Feng et al.,2010; Atkins et al., 2014); however, Mg-buserite is not stable and can transform to 0.7 nm birnessite when dehydrated. For the identification of todorokite,

the synthetic sample was heated for 12 h at 140 °C before XRD analysis to exclude the presence of Mg-buserite.

For transmission electron microscopy (TEM) imaging, the sample was gently ground to powder and dispersed in absolute alcohol via sonication. Then, the sample was loaded on a holey carbon TEM grid. Imaging was performed at an accelerating voltage of 200 kV on an FEI Tecnai (F20) microscope. The specific surface area of the synthetic todorokite is 209 ± 4 (2SD, n = 5) $m^2\ g^{-1}$, as measured by the N_2 Brunauer-Emmet-Teller (BET) method.

2.2. Adsorption experiments

All reagents used in this study were of reagent grade. Distilled DI water (>18.2 MΩ) was used for all experiments. The Zn stock solution (35 mM) used in this study was prepared from $Zn(NO_3)_2 \cdot 6H_2O$ (CAS: 10196-18-6, Sigma–Aldrich) and DI water. The acids used in all experiments were purified via double subboiling distillation. The labware used in the adsorption and isotopic experiments was made of Teflon material to minimize Zn contamination.

Two types of Zn adsorption experiments were carried out under ambient environmental conditions: (i) kinetic adsorption experiments (duration of 0.5−120 h) and (ii) adsorption edge experiments from pH 3 to 9. For the kinetic adsorption experiments, suspensions of 0.4 g L^{-1} todorokite were equilibrated at pH 6 for 24 h in 0.1 M $NaNO_3$ solution while constantly stirring. After this pre-equilibration step, the necessary amount of Zn from the $Zn(NO_3)_2$ stock solution was added to achieve an initial Zn concentration of 0.05 mM. After a reaction time of 0.5 to 120 h, the solid and liquid phases were separated by centrifugation. The supernatants were passed through a methacrylate butadiene styrene filtration assembly with a polyethersulfone (PES) membrane and 0.22 μm pores (Sartorius, Germany) and analyzed for Zn using inductively coupled plasma-optical emission spectroscopy (Thermo ICP 6000 series ICP–OES).

For the adsorption edge experiments, prior to Zn addition, todorokite powder was suspended for 24 h at a fixed pH (3 to 9) at three different ionic strengths (I = 0.001, 0.01 and 0.1 M $NaNO_3$). Then, small amounts of $Zn(NO_3)_2$ stock solution were added dropwise to todorokite suspensions to achieve initial Zn concentrations of 0.05 and 0.2 mM. These initial Zn concentrations were selected because the concentrations of Zn adsorbed on todorokite (0.002 < Zn/Mn atomic ratio < 0.052) covered the range

of Zn contents found in marine Mn-rich sediments such as ferromanganese crusts and nodules (0.001 < Zn/Mn atomic ratio < 0.007) (Manheim and Lane-Bostwick, 1991; Little et al., 2014). While adding Zn, the suspension was stirred vigorously to avoid the formation of Zn precipitates due to local oversaturation of the suspension. The solid/liquid ratio was set equal to 0.4 g $L^{-1,}$ and the pH of all adsorption experiments was adjusted to the desired value by the addition of 0.01 M $NaOH/HNO_3$. Based on the kinetic experiments, the reaction time for adsorption edge experiments was set to 48 h to ensure equilibrium. After 48 h, the solid and liquid phases were separated by centrifugation, and the supernatant was further filtered through a methacrylate butadiene styrene filtration assembly with a polyethersulfone (PES) membrane and 0.22 μm pores (Sartorius, Germany). The Zn concentration in the supernatants was measured by inductively coupled plasma-optical emission spectroscopy (Thermo ICP 6000 series ICP–OES). The dominant Zn species in the adsorption experiments was calculated using Visual MINTEQ.3.1 and found to be Zn^{2+} across the pH range 3 – 9 (Fig. S1). The Zn surface coverage was calculated from the difference in concentrations between the initial and equilibrium solutions by taking into account the surface area of todorokite and the solid/liquid ratio. Blank experiments with no Zn added to the reacting suspension of todorokite were performed to monitor the external Zn contamination during adsorption experiments. All the experimental data are averages of duplicates, and the relative errors are less than 5%.

2.3. Zn stable isotope measurements

Isotopic samples were obtained after the batch adsorption experiments. Solid samples separated by centrifugation were dissolved in 11 M HCl and heated at 100 °C in sealed Teflon vials for 3 h to extract the adsorbed Zn. The amount of aqueous Zn remaining in the solids after centrifugation was less than 1‰ of the adsorbed Zn, according to the estimation of the Na content extracted by this step and the Na/Zn ratio of the supernatant (Gou et al., 2018). The digested solutions from the solids and the supernatants obtained after various adsorption experiments were evaporated to dryness and redissolved three times in 11 M HCl to convert Zn to a chloride form. After that, each residue was dissolved in a 2 M HCl solution and loaded on columns filled with AG MP-1 anion-exchange resin (100–200 mesh; Bio–Rad, USA). Samples were purified following the procedure described by Gou et al. (2018). Column yields were measured after Zn purification and determined to be 100 ± 6%. Total procedural blanks of

Zn were analyzed for each experimental run and were found to be less than 20 ng, which was negligible (< 0.1%) compared to the ~20 μg Zn in each sample. After purification, the samples were evaporated to dryness and dissolved in 0.05 M HNO_3. Aliquots of varying volumes of this Zn solution were sampled to obtain a final 0.05 M HNO_3 solution with 0.5 ppm Zn and 0.2 ppm Cu NIST 647. Cu NIST 647 and Zn (high purity in-house standard) mixed standard solutions with equivalent Cu/Zn ratios of samples were also prepared to run alternatively with the samples to correct the instrumental mass bias (Marechal et al., 1999).

The Zn isotopic ratio was measured using a Neptune Plus (Thermo Fisher Scientific) MC-ICP–MS at the Isotope Geochemistry Lab of Nanjing University. The instrument was run in "wet-plasma" mode at low mass resolution (M/ΔM = 400) using a free aspirating glass expansion nebulizer. Prior to isotopic composition measurement, a 0.05 M HNO_3 solution was introduced before each isotope ratio measurement to make the baseline decrease to a constant value. Then, a 40 s on-peak blank of 0.05 M HNO_3 was measured for background subtraction. Each measurement consisted of three blocks of 60 cycles (60 s for each cycle). The signal of ^{62}Ni was collected to correct for isobaric interference on ^{64}Zn from ^{64}Ni, while the impact on the quality of the ^{64}Zn MC-ICP–MS signal was found to be negligible due to effective chromatography.

The Zn isotopic compositions of all samples were reported relative to the in-house standard as:

$$\delta^{66}Zn = ((^{66}Zn/^{64}Zn)_{sample}/(^{66}Zn/^{64}Zn)_{HPS}) - 1) \times 1000\ (‰) \qquad (1)$$

The in-house standard was calibrated with respect to IRMM 3702 and JMC Lyon international standards, giving $\delta^{66}Zn_{HPS}$=−0.36 ± 0.03‰ and $\delta^{66}Zn_{HPS}$=−0.09 ± 0.03‰, respectively (Gou et al., 2018). The long-term external reproducibility of the $^{66/64}Zn$ ratio measurement by MC-ICP–MS was better than 0.03‰ (2 SD) based on repeat analysis of a standard solution and geological standards over a period of 3 years. The measured $\delta^{66}Zn$ values of two reference materials (i.e., Nod-P-1, BCR) are consistent with those reported in the literature, attesting to the accuracy of the analytical procedure (Marechal et al., 1999; Bryan et al., 2015; Gou et al., 2018). The isotopic fractionation of Zn ($\Delta^{66}Zn_{adsorbed\text{-}aqueous}$) between the solid phase and aqueous phase is defined as:

$$\Delta^{66}Zn_{adsorbed\text{-}aqueous} = \delta^{66}Zn_{adsorbed} - \delta^{66}Zn_{aqueous} \qquad (2)$$

The mass balance offset was calculated as follows:

$$Offset = \delta^{66}Zn_{stock} - (\delta^{66}Zn_{adsorbed} \times \%\ adsorbed + \delta^{66}Zn_{aqueous}(100 - \%\ adsorbed)) \qquad (3)$$

2.4. EXAFS sample preparation and data analysis

EXAFS samples were prepared in the same manner as the isotopic experiments, with a large vessel to yield at least 20 mg of solid for analysis. The reaction conditions, including the solid/liquid ratio, initial Zn concentration, ionic strength, and pH, were kept the same as those of the corresponding isotopic samples. The samples for EXAFS analysis were prepared as fresh wet pastes and stored in a refrigerator prior to EXAFS analysis.

The Zn *K*-edge EXAFS data for adsorption and standard samples were collected at the 1W1B beamline of Beijing Synchrotron Radiation Facility (BSRF, China) and BL12C in Photon Factory (PF) synchrotron-radiation facility within the National Laboratory for High Energy Physics (KEK), Tsukuba, Japan. The electron storage ring operated at 2.5 GeV with an average beam current of 200 mA in BSRF and at 2.5 GeV with a maximum beam current of 450 mA in PF. A pair of Si(111) crystals were employed as a monochromator, which was detuned by 30% to reject X-ray harmonics. The spectra of all samples were measured by both transmission and fluorescence mode simultaneously, and the fluorescence data were recorded using a multichannel Ge detector. The X-ray energy was calibrated with a Zn metal foil, and the first inflection point in the Zn K-edge was set to 9659 eV. An Fe metal filter was used to dampen the fluorescence of Mn. Because of the fluorescence of Mn, a minimum of three scans were collected for each sample to obtain a good signal/noise ratio. Concentrated samples and standards were analyzed in transmission mode.

The Zn EXAFS spectra were processed and analyzed using an IFEFFIT 1.2.11 program package for data normalization and Fourier transformation (Ravel and Kelly, 2007). The $\chi(k)$ spectra were k^3-weighted and Fourier transformed (FT) over the k range 3−12 $Å^{-1}$. Shell-by-shell fitting was performed in R-space to obtain detailed local structural information. Theoretical backscattering-amplitude and phase-shift values were calculated based on the crystal structures of $Zn(NO_3)_2$ and todorokite model clusters. During sample spectra processing, the coordination number N, the distance R, and the Debye–Waller factor σ^2 were allowed to float as adjustable parameters, and a single energy shift ΔE_0 was used for all shells. The number of adjustable parameters in the fitting procedures did not exceed the maximum number of independent parameters. The quality of each fit was evaluated quantitatively with the reduced chi square and R-factor parameters. The amplitude reduction factor (S_0^2) was estimated to be 0.97 based

on the fitting of a $Zn(NO_3)_2$ solution standard and was then applied to the adsorption samples.

2.5. Density functional theory calculations

Initial Zn-todorokite models were created by expansion of the experimental unit-cell structure of todorokite mineral (Post et al., 2003) to a 1 × 2 × 1 supercell, which contained one or two Zn cations per eight H_2O molecules in each tunnel space ($ZnMn_{12}O_{24}\cdot 8H_2O$ or $Zn_2Mn_{12}O_{24}\cdot 8H_2O$). Water molecules were initially placed at the corner sites in the tunnel according to X-ray structure refinement results (Post et al., 2003), while Zn cations were placed at the center or corner sites in the tunnel. Mn(III) cations are believed to occupy the larger corner-sharing octahedra of todorokite (Post et al., 2003). In the current models, two or four corner-sharing Mn octahedra sites were imposed by the electron configuration of Mn(III), with the other sites imposed by Mn(IV). After relaxation of the structures, the magnetic moments of Mn(IV) and Mn(III) sites were 2.9–3.1 and 3.7–3.8 μ_B. For aqueous Zn^{2+}, we constructed a cluster model of Zn^{2+} surrounded by one shell or two shells of H_2O molecules [$Zn^{2+}\cdot 6(H_2O)$ or $Zn^{2+}\cdot 18(H_2O)$] in a 30 × 30 × 30 Å periodic box based on the symmetry reported in Ducher et al. (2018).

All DFT calculations were performed using the CASTEP code (Clark et al., 2005) under the spin-polarized generalized gradient approximation (GGA) with the Perdew–Burke–Ernzerhof (PBE) functional (Perdew et al., 1996). The valence electron states of the Mn, Zn, O, and H ultrasoft pseudopotentials (Vanderbilt, 1990) were $3s^2 3p^6 3d^5 4s^2$, $3d^{10}4s^2$, $2s^2 2p^4$, and $1s^1$, respectively. The kinetic energy cutoff was 500 eV. The *k*-point grid for the first Brillouin zone (Monkhorst and Pack, 1976) was 1 × 1 × 1 for aqueous Zn^{2+} models and 4 × 10 × 4 for Zn-todorokite models. The calculated atomic force converged to less than 0.01 eV/Å. The magnetic ordering among edge-sharing Mn octahedra was ferromagnetic, but the ordering between the corner-sharing of the triple chains of edge-sharing octahedra was antiferromagnetic (Kaltak et al., 2019). Geometry optimizations were performed with no symmetry imposed until the following conditions were met: total energy ≤ 0.000005 eV, atomic forces ≤ 0.05 eV/Å (≤ 0.005 eV/Å for aqueous Zn^{2+} models), stress ≤ 0.03 GPa and atomic displacement ≤ 0.0005 Å. All atomic coordinates were fully relaxed, while $\alpha = \gamma = 90°$ was fixed in todorokite models, and the supercell size was fixed in aqueous Zn^{2+} models. The crystal structures were rendered using VESTA software (Momma and Izumi, 2011).

The $^{66}Zn/^{64}Zn$ reduced partition function ratios (β-factors) of Zn-bearing todorokite were calculated with harmonic vibrational frequencies based on the high-temperature product rule (Bigeleisen and Mayer, 1947; Schauble, 2004; Blanchard et al., 2017):

$$\beta = \left[\prod_{i=1}^{3N_{at}} \prod_{q} \frac{v^*_{q,i}}{v_{q,i}} \frac{e^{-hv^*_{q,i}/(2kT)}}{1-e^{-hv^*_{q,i}/(kT)}} \frac{1-e^{-hv_{q,i}/(kT)}}{e^{-hv_{q,i}/(2kT)}} \right]^{1/(N_q N)} \quad (4)$$

where v is the harmonic vibrational frequency of the ith vibrational mode at a phonon wave vector q; h, k_B, and T are the Planck constant, Boltzmann constant, and absolute temperature in Kelvin, respectively; N_{at}, N_q, and N represent the number of atoms in a calculated model, the number of phonon wave vectors, and the number of sites of isotopes, respectively; and * represents a frequency for a heavier isotope (^{66}Zn in this study). The harmonic vibrational frequencies were obtained only at the gamma point by phonon calculations based on a finite displacement method (Ackland et al. 1997; Parlinski et al. 1997), which is implemented in CASTEP; in Eq. (4), N_q was 1, and the ith vibrational mode started from 4. The $^{66}Zn/^{64}Zn$ equilibrium isotopic fractionation factor between Zn-adsorbed todorokite and aqueous Zn^{2+}, $\Delta^{66}Zn_{adsorb-aq}$, was obtained by combining the corresponding β-factors of the solid phase and aqueous Zn^{2+}.

3. Results

3.1 Characterization of synthetic todorokite

The XRD pattern of the synthetic todorokite sample is shown in Fig. 1a. It shows well-resolved diffraction peaks at ~9.6 Å (001), ~4.8 Å (002), 3.2 Å (003), ~2.5 Å (210), ~2.4 Å (21–1), ~2.2 Å (21–2), ~1.9 Å (31–2), ~1.7 Å (21–4), ~1.5 Å (21–5) and ~1.4 Å (020). These peaks are consistent with those of typical todorokite (JCPDS 38-0475) and naturally formed todorokites (Post et al., 2003; Feng et al., 2004; Bodei et al., 2007; Manceau et al., 2007; Atkins et al., 2014; Wu et al., 2019). Fig. 1b and c show the morphology of synthetic todorokite by TEM observation. The particles of synthetic todorokite exhibit fibrous laths aligned with each other at 120° to form large aggregates (Fig. 1b). From the lattice image of the synthetic todorokite (Fig. 1c), we observe that the todorokite fibers elongate longitudinally along the (010) direction. Ideal todorokite exhibits lattice fringes with fringe widths (along the (001) direction) of ~1 nm corresponding to a 3 × 3 MnO_6 octahedra tunnel size. However,

tunnels of different MnO_6 octahedral fringe widths along the (001) direction have been observed (Fig. 1c). This indicates that in the trilling intergrowths, the tunnel size along the (001) direction is variable. Such morphologies (fibrous and trilling patterns) and intergrowths are the typical characteristics of natural todorokite, consistent with previously reported synthetic and natural todorokites (Feng et al., 2004; Bodei et al., 2007; Manceau et al., 2007; Atkins et al., 2014; Wu et al., 2019).

3.2 Zn adsorption onto todorokite

Fig. 2a shows Zn adsorption ($[Zn]_{initial}$ = 0.05 mM) as a function of pH for three different ionic strengths (0.005, 0.01, 0.1 M $NaNO_3$). A substantial increase in Zn adsorption from 0.11 μmol m^{-2} to 0.60 μmol m^{-2} occurs over the pH range from 3 to 9. Clearly, there is an ionic strength effect, with the highest Zn adsorption in 0.005 M $NaNO_3$ solution over most of the pH range. Similar evolution is observed when studying Zn adsorption from solution as a function of pH for an initial Zn concentration of 0.2 mM (Fig. 2b). A substantial increase in Zn adsorption from 0.36 μmol m^{-2} to 2.39 μmol m^{-2} occurs over the pH range from 3 to 9. Zn adsorption significantly varies with ionic strength between 0.005 and 0.1 M $NaNO_3$, with the highest Zn adsorption in 0.005 M $NaNO_3$ solution. Such ionic strength effects on Zn adsorption to other mineral surfaces have also been reported (Guinoiseau et al., 2016; Nelson et al., 2017). This ionic strength-dependent behavior of Zn adsorption suggests that the formation of outer-sphere surface complexes is the predominant adsorption mechanism, especially at pH 3−7 (Strawn and Sparks, 1999; Elzinga et al., 2002). Since Na^+ ions in the background electrolyte can compete with Zn adsorption for these relatively weak adsorption sites, less Zn will be adsorbed when the ionic strength increases. To confirm that outer-sphere Zn adsorption complexes formed on todorokite, EXAFS analyses were performed (see section 3.3).

The results of time series experiments of Zn adsorption to todorokite are presented in Fig. 3a. Zn adsorption is initially fast, with 30% of total Zn removed from solution in the first 15 min. Thereafter, Zn adsorption slows slightly and remains almost constant from 24 to 120 h. After 120 h of reaction time, approximately 50% of total Zn is adsorbed, resulting in a surface coverage of 0.29 μmol m^{-2}. These results suggest that the adsorption equilibrium between todorokite and the reacting solution is achieved after 24 h of reaction time.

3.3 Zn isotope fractionation during the adsorption process

The Zn isotopic compositions of the adsorbed and aqueous phases in the time series experiments are plotted in Fig. 3b and tabulated in Table 2. The initial isotopic composition (δ^{66}Zn) of the Zn stock solution is 0.28 ± 0.06‰ (2SD, n = 6). In the time series experiments, light Zn isotopes are preferentially partitioned to the solid phase, and heavy isotopes remain in solution. During the first 12 h, the δ^{66}Zn values of the aqueous phase show a rapid decrease from 0.38‰ ± 0.06 to 0.28 ± 0.04‰, while simultaneously, the δ^{66}Zn values of adsorbed Zn increase from 0.23 ± 0.05‰ to 0.29 ± 0.01‰. From 24 h to 120 h, no significant changes in the δ^{66}Zn values of the aqueous and adsorbed phases are observed. The Zn isotope fractionation between adsorbed and aqueous phases ($\Delta^{66}Zn_{adsorbed\text{-}aqueous}$) evolves during the first 12 h from −0.15 ± 0.08‰ to −0.06 ± 0.04‰ and remains nearly unchanged for longer reaction times (Fig. 3c and Table 2). This suggests that isotopic equilibrium between adsorbed and aqueous Zn was achieved after ~ 12 h of reaction.

The pH series experiments were conducted at different initial Zn concentrations of 0.05 and 0.2 mM, and the results are presented in Fig. 4 and Table 2. In the experiments of $[Zn]_{initial}$ = 0.05 mM, light Zn isotopes are preferentially partitioned to the solid phase relative to the aqueous phase (Fig. 4a). The Zn isotopic compositions of the adsorbed phase remain almost constant at approximately 0.2 ± 0.02‰ at pH 3 to 5 and increase from 0.26 ± 0.01‰ to 0.29 ± 0.01‰ when pH values increase from 6 to 9. Aqueous compositions are almost identical within analytical uncertainties over the pH range from 3 to 8. It should be noted that the Zn isotope composition of the aqueous phase at pH 9 is absent because aqueous Zn remaining in solution is below the detection limit owing to the nearly 100% Zn uptake under this condition. Overall, Zn isotope fractionation between the adsorbed and aqueous phases is slightly negative for the initial Zn concentration of 0.05 mM, and the average $\Delta^{66}Zn_{adsorbed\text{-}aqueous}$ for all 12 samples is –0.07 ± 0.04‰ (Fig. 4b).

In the experiments of $[Zn]_{initial}$ = 0.2 mM, Zn isotope fractionation behavior can be divided into two pH groups (Fig. 4c). From pH 3 to 6, the Zn isotope compositions and evolution of the adsorbed and aqueous phases are similar to those in the experiments with $[Zn]_{initial}$ = 0.05 mM. A continual enrichment in light isotopes in the adsorbed phase and heavy isotopes in the solution is observed. At pH 7 to 8, heavy Zn isotopes are preferentially partitioned onto the adsorbed phase relative to the aqueous solution. The enrichment of heavy isotopes on todorokite, which is not observed in the

experiments of $[Zn]_{initial}$ = 0.05 mM, seems to imply that relatively high Zn concentrations may induce different Zn isotope fractionation. The Zn isotopic fractionation value ($\Delta^{66}Zn_{adsorbed\text{-}aqueous}$) is calculated to be −0.08 ± 0.03‰ in the pH 3 to 6 experiments, while the $\Delta^{66}Zn_{adsorbed\text{-}aqueous}$ value increases to 0.05 ± 0.05‰ in the pH 7 to 8 experiments (Fig. 4d). Mass balance calculations are applied for almost all samples to assess the success of the experiments and exclude the possibility of external contamination. The mass balance offset is calculated according to the equation ($\delta^{66}Zn_{aqueous}$ (1−% adsorbed) +$\delta^{66}Zn_{adsorbed}$ % adsorbed) − $\delta^{66}Zn_{stock}$. These values are within ± 0.05‰ of the Zn isotope composition of the starting stock solution (Table 2), indicating that the experimental data are reliable.

3.4 Zn surface speciation as revealed from EXAFS

Fig. 5a shows the background subtracted k^3-weighted EXAFS spectra (χ function) for the Zn-todorokite samples and three Zn reference compounds (e.g., Zn solution, Zn hydroxide ($Zn(OH)_2$), and hydrozincite ($Zn_3(OH)_6(CO_3)_2$)). The EXAFS spectra of the Zn-adsorbed todorokite samples show a distinct change with pH. The samples prepared at pH 3 with Zn concentrations of 0.05 and 0.2 mM yield similar EXAFS oscillations, which are almost identical to the EXAFS of the $Zn(NO_3)_2$ solution. Correspondingly, Fig. 5b shows the Fourier transformed spectra (uncorrected for phase shift) for the Zn-todorokite samples, where only a single peak is observed. This peak results from O backscattering in the first coordination shell of the Zn atoms. The fit results for the Zn-todorokite samples and the reference compounds are presented in Table 3, resulting in bond distances of ~2.06 Å and coordination numbers of 5.8−6.2. Fitting of the $Zn(NO_3)_2$ solution EXAFS data results in a bond distance of 2.06 Å and coordination number of 6, which are in good agreement with many previous studies (Bochatay and Persson, 2000; Roberts et al., 2003; Nelson et al., 2017; Gou et al., 2018). At pH 3, the similarity between the Zn adsorption structure and aqueous Zn aqua cation provides strong evidence for the formation of an outer-sphere surface complex, in agreement with the marked ionic-strength dependent adsorption behavior observed at pH 3 (Fig. 2).

Compared to the pH 3 samples, the samples prepared at pH 6 and 8 with initial Zn concentrations of 0.05 and 0.2 mM exhibit slightly different features at higher k values between 7 and 8.5 $Å^{-1}$, suggesting a change in the mechanism of surface complexation (Fig. 5a). In the Fourier transform, the first shell O atoms are dominated by a major peak that shifts to lower values. This indicates that the

bond length between Zn and O (R_{Zn-O}) in these samples is shorter than that of Zn in solution. Further shells at higher R are observed, indicating the presence of backscatterer second shell atoms residing at longer distances, such as Zn and/or Mn. The presence of backscatterer second shell atoms suggests that Zn either forms covalent bonds with todorokite surface sites or precipitates. Shell-by-shell fits for these samples exhibit EXAFS contributions from the first shell Zn−O scattering as well as second shell Zn−Zn/Mn scatterers. The fit of the first shell yields R_{Zn-O} = 2.00−2.05 Å and coordination numbers (CN) ranging from 4.8–5.5. The bond distances for the O shell at R_{Zn-O} = 2.00−2.05 Å are similar to those found for the hydrozincite ($Zn_5(CO_3)_2(OH)_6$) sample (R_{Zn-O} ~ 2.00 Å, see Table 4), where Zn forms a mixture of octahedrally and tetrahedrally coordinated complexes. Bochatay and Persson (2000) found that Zn surface complexes adsorbed on manganite had Zn–O bond distances of approximately 1.98 to 2.04 Å and that these distances are consistent with the formation of a mixture of octahedral and tetrahedral complexes. Similar observations for Zn adsorption on other mineral surfaces have also been reported (Waychunas et al., 2002; Cismasu et al., 2013; Nelson et al., 2017; Gou et al., 2018). Therefore, for the Zn adsorbed todorokite samples prepared at pH 6 and 8, the Zn–O bond distances between 2.00–2.05 Å are indicative of a mixture of octahedrally and tetrahedrally coordinated structures.

To fit the second shell for the pH 6 and 8 samples, we tested both Zn−Zn and Zn−Mn paths. Because of the similar backscatter power between Zn and Mn, either Zn−Zn or Zn−Mn paths can fit the second shell, yielding an interatomic distance of 3.10−3.14 Å and CN of 1.5–3.0. Due to the high uncertainty in the higher shell coordination number in fitting EXAFS spectra (Ravel and Kelly, 2007), bond distance was used to assess the local structure of Zn on todorokite. If a Zn−Zn path is assumed, the Zn−Zn distance is 3.10−3.14 Å, which is similar to that of hydrozincite ($Zn_5(CO_3)_2(OH)_6$), where a distance of 3.12 Å is fitted, and much shorter than the Zn−Zn bond distance (3.23 Å) in Zn hydroxide ($Zn(OH)_2$) (Table 3). However, precipitated or polymerized Zn as either hydrozincite or Zn hydroxide at pH 6 is highly unlikely (Fig. S1) because of the low pH (below neutral) and low Zn concentration (Bochatay and Persson, 2000). Thus, Mn backscattering seems more reasonable, and a good fit with a Zn−Mn distance of 3.10−3.14 Å (Table 3) suggests the formation of an inner-sphere surface complex structure.

3.5 Theoretical calculation of the stable isotope fractionation

In the DFT geometry optimizations, the coordination structure of Zn cations in the tunnel strongly depends on the cation content and position (Table 4), while the lattice parameters of Zn todorokite models show minimal changes depending on the cation content. The calculated lattice parameters (a = 10.1, b = 2.88, c = 9.67 Å, β = 95.6°) differ by less than 1.2–3.5% from the experimental results (a = 9.76, b = 2.84, c = 9.56 Å, β = 94.2°; Feng et al., 2004). The atomic coordinates of the geometry-optimized structures are provided in Table S1. In $ZnMn_{12}O_{24}\cdot 8H_2O$ models, Zn forms octohedral coordination with six H_2O molecules (i.e., outer-sphere surface complexes) at the center of the tunnel (model 1); at the corners, Zn forms tetrahedral coordination with two H_2O molecules and two surface O molecules (i.e., inner-sphere surface complexes; model 2). The d<Zn-O> of octahedral Zn is larger than that of tetrahedral Zn (2.09 vs. 1.96 Å). In $Zn_2Mn_{12}O_{24}\cdot 8H_2O$ models, two hydrated Zn cations cannot occupy the center sites at the same time because of limited space. If one Zn occupies the center site, the other Zn should occupy the corner site (model 3); otherwise, both Zn cations occupy the corner sites (model 4) to minimize repulsion among tunnel cations (Fig. 6). In model 3, we find octahedral Zn at the corner site, coordinated with one H_2O and five surface O (i.e., octahedral inner-sphere surface complexes), at d<Zn-O> = 2.17 Å (Table 4). The presence of octahedral Zn at the corner site also increases the d<Zn-O> of the outer-sphere complex of Zn at the center from 2.09 to 2.14 Å. In model 4, both Zn cations form tetrahedral coordination at the corners, with a slight increase in d<Zn-O> from 1.96 to 1.98 Å. Based on the current DFT calculations, octohedrally coordinated Zn shows a wider range of d<Zn-O> from 2.09 to 2.14 Å than tetrahedrally coordinated Zn (1.96–1.98 Å). Based on the geometry–optimized structures, the beta factors ($10^3 \ln\beta$ $^{66}Zn/^{64}Zn$) calculated at 300 K are 2.8–3.3‰ for octahedral Zn and 3.5–3.9‰ for tetrahedral Zn (Fig. 6).

The d<Zn-O> of $Zn^{2+}\cdot 6(H_2O)$, a simple model for aqueous Zn^{2+}, is calculated to be 2.12 Å (Table 4). This distance is slightly overestimated by 2.9% compared to the distance of aqueous Zn^{2+} obtained by the current EXAFS analysis (2.06 Å; Table 3). On the other hand, when a larger cluster model including double hydration shells, $Zn^{2+}\cdot 18(H_2O)$, is geometry optimized, d<Zn-O> is calculated to be 2.17 Å. This distance is consistent with the result of a recent DFT study, in which DFT-based MD simulations of a periodic $Zn^{2+}\cdot 64(H_2O)$ model predict 2.17 Å for d<Zn-O> for aqueous Zn^{2+} (Ducher et al., 2018). However, the DFT method with more realistic aqueous Zn^{2+} models used in the current study and Ducher et al. (2018) predict d<Zn-O> to be even longer than the distance of the simple

$Zn^{2+}\cdot 6(H_2O)$ cluster model (~5% error compared to the experimental value). Because the level of accuracy of DFT in prediction of the bond distances of cations differs between aqueous and solid phases, careful interpretation is required for direct comparison of the *d*<Zn-O> for the solid and aqueous phases and hence the beta factors between them. When the beta factor of $Zn^{2+}\cdot 6(H_2O)$ is used for aqueous Zn^{2+}, the $^{66}Zn/^{64}Zn$ equilibrium isotopic fractionation factor between adsorbed Zn and aqueous Zn^{2+} ($\Delta^{66}Zn$) is –0.2 to –0.3‰ for octahedral Zn cations and +0.5 to +0.8‰ for tetrahedral Zn in todorokite.

4. Discussion

4.1 Constraining Zn isotope fractionation factors

In the experiments at pH values of 3.0 to 6.0 and Zn concentrations of 0.05−0.02 mM, both $\delta^{66}Zn_{adsorbed}$ and $\delta^{66}Zn_{aqueous}$ showed a linear increase as the proportion of adsorbed Zn increased (Fig. 7a). Equilibrium and Rayleigh fractionation models are used to fit our experimental data. In the equilibrium fractionation model, adsorbed Zn can still isotopically exchange with aqueous Zn irrespective of the degree of adsorption. In the Rayleigh fractionation model, Zn is separated from the aqueous solution to the solid phase during adsorption, and adsorbed and aqueous Zn do not isotopically equilibrate with one another. The two models are described based on the following equations:

Equilibrium model: $$\delta^{66}Zn_{aqueous} = \frac{\delta^{66}Zn_{stock} - 1000 \times f \times (\alpha_{adsorbed-aqueous} - 1)}{1 - f + (f \times \alpha_{adsorbed-aqueous})} \quad (5)$$

Rayleigh model: $$\delta^{66}Zn_{aqueous} = (1000 + \delta^{66}Zn_{stock})(1 - f)^{(\alpha_{adsorbed-aqueous} - 1)} - 1000 \quad (6)$$

where f is the fraction of Zn sorbed, and $\alpha_{adsorbed\text{-}aqueous}$ is the estimated isotopic fractionation factor between adsorbed and aqueous Zn. The $\delta^{66}Zn_{stock}$ is the measured value (0.28 ± 0.06‰) of the initial aqueous Zn. An $\alpha_{adsorbed\text{-}aqueous}$ of 0.9999 is obtained from linear regression of the experimental data. The $\delta^{66}Zn_{aqueous}$ and $\alpha_{adsorbed\text{-}aqueous}$ values are used to predict the corresponding $\delta^{66}Zn_{adsorbed}$ on the todorokite surface according to Eq. (3).

$$\delta^{66}Zn_{adsorbed} = \alpha_{adsorbed-aqueous}\left(\delta^{66}Zn_{aqueous} + 1000\right) - 1000 \quad (7)$$

Fig. 7a shows that the equilibrium fractionation model fits our experimental data better than the Rayleigh model, indicating adequate isotope exchange between the aqueous solution and the todorokite surface throughout the adsorption reactions. This equilibrium fractionation during adsorption reactions is in full agreement with that reported in studies for Zn and other metal adsorption (e.g., Cd, Li, Cu,

Mo) on mineral surfaces (Barling and Anbar, 2004; Wasylenky et al., 2008; Wasylenky et al., 2014; Gou et al., 2018).

Finally, the isotopic fractionation between adsorbed and aqueous Zn ($\Delta^{66}Zn_{adsorbed\text{-}aqueous}$) is obtained from isotopic fractionation factors ($\alpha_{adsorbed\text{-}aqueous}$) following Eq. (4).

$$\Delta^{66}Zn_{adsorbed-aqueous} \cong 1000 \times ln\alpha_{adsorbed-aqueous} \quad (8)$$

This calculation yields a $\Delta^{66}Zn_{adsorbed\text{-}aqueous}$ value equal to –0.10 ± 0.04‰, consistent with the average (–0.11 ± 0.04‰) from the measured $\Delta^{66}Zn_{adsorbed\text{-}aqueous}$ value.

In the adsorption experiments at pH values of 7.0 to 8.0 and Zn concentrations of 0.05−0.2 mM, Zn isotope compositions of solid and aqueous phases do not change within analytical error with respect to the fraction of adsorbed Zn (Fig. 7b). This relatively constant fractionation between solid and aqueous phases indicates achievement of isotopic equilibrium. This result is in agreement with our time series experiments, which show that Zn isotope fractionation during adsorption on todorokite reaches equilibrium at approximately 12 h (see section 3.3). Previous studies also suggest that equilibrium of Zn isotopes is achieved within a few hours of adsorption to mineral surfaces of 2-line ferrihydrite, calcite, quartz and amorphous silica (Juillot et al., 2008; Dong et al., 2016; Nelson et al., 2017).

To summarize, different magnitudes for Zn isotope fractionation during adsorption to todorokite under different pH values are observed. The $\Delta^{66}Zn_{adsorbed\text{-}aqueous}$ values of –0.10 ± 0.04‰ and 0.05 ± 0.05‰ are calculated for pH 3.0 to 6.0 and pH 7.0 to 8.0, respectively. Such differences under different pH values are related to different Zn surface speciation, as detailed in the following section.

4.2 Effect of Zn speciation on Zn isotope fractionation

The distinct Zn isotope fractionation behaviors under different pH values (Fig. 7) might be explained by two main processes: i) isotopic fractionation arises during the exchange of isotopes among different Zn species in solution; ii) fractionation occurs between dissolved and adsorbed Zn species at the mineral-solution interface.

Regarding the first process, aqueous Zn speciation for the adsorption edge experiments with Zn concentrations of 0.05 and 0.2 mM was calculated using Visual MINTEQ 3.1 (Fig. S1). Calculations show that $Zn(H_2O)_6^{2+}$ is the main species (91.5%) with only a minor amount (8.5%) of $ZnNO_3(H_2O)_5^{+}$ at pH < 8 (the major pH range used in the adsorption experiments). At low ionic strength (e.g., 0.001

M $NaNO_3$), the proportion of $ZnNO_3(H_2O)_5^+$ is even smaller. A number of studies based on ab initio calculations report the values of reduced partition function ratios (as 1000lnß) for various Zn species in solution (Pye et al., 2006; Fujii et al., 2010; Fujii et al., 2014). Zn–Cl complexes, for example, are reported to incorporate lighter isotopes, with 1000 lnß values ranging from 2.293–3.136 as the number of Cl^- ligands in the complex increases, compared with 3.263 for $Zn(H_2O)_6^{2+}$ (Fujii et al., 2010). The magnitudes of fractionation from $Zn(H_2O)_6^{2+}$ for chloro complexes translate to values of $\Delta^{66}Zn_{hexaquo-chloro}$ ranging from 0.13‰ for $ZnCl(H_2O)_5^+$ to 1.40‰ for $ZnCl_4^{2-}$. Fujii et al. (2014) also estimated the lnß of carbonate complexes of Zn to be 3.877 for $ZnHCO_3^-$ and 4.199 for $ZnCO_3^0$ and predicted that carbonate complexes should be associated with a relatively heavy pool of Zn in aqueous solution. Similarly, $ZnSO_4^{0,}$ which comprises a heavy pool of Zn by 0.3‰ relative to $Zn(H_2O)_6^{2+}$, has been reported (Fujii et al., 2014). Thus, the formation of $ZnNO_3(H_2O)_5^+$ may cause isotopic fractionation from $Zn(H_2O)_6^{2+}$. While the 1000 lnß value for $ZnNO_3(H_2O)_5^+$ is currently unknown, the fractionation factors for Zn-ligand complexes may be predicted according to a positive correlation between the complexation constant (log*K*) and isotopic fractionation (Ryan et al., 2014; Markovic et al., 2017). Based on the small log*K* (0.4) and low proportion (8.5%) of $ZnNO_3(H_2O)_5^+$ under the experimental conditions (Allison et al., 1991), we surmise that the formation of $ZnNO_3(H_2O)_5^+$ does not significantly contribute to the measured Zn isotope fractionation. Further studies on the calculation of this species would be useful to test this hypothesis.

Regarding the second process, adsorption of aqueous species to mineral surfaces is often accompanied by a change in the chemical bond stiffness of the element of interest, which stems from a different molecular structure (surface speciation) of Zn and would thus cause isotopic fractionation. As Zn is naturally present only as divalent Zn and is insensitive to redox, the coordination number is proposed to be an important factor in controlling the vibrational frequencies (i.e., stiffness) of Zn-oxygen bonds (Schauble, 2004). Thus, coordination number changes have been used to explain Zn isotope fractionations during adsorption, where essentially heavy Zn isotopes are found to be more likely enriched in structures with low coordination numbers in which Zn has stiffer bonds (Schauble, 2004). In this study, outer-sphere Zn complexes at low pH values (e.g., pH 3) on todorokite concentrate slightly lighter Zn compared to the aqueous phase ($\Delta^{66}Zn_{adsorbed-aqueous}$ = ~ –0.1 ± 0.04‰) (Fig. 8), although the structure of Zn in aqueous solution and Zn in an outer-sphere complex on todorokite are

very similar, with Zn surrounded by approximately six water molecules. According to DFT calculations, outer-sphere octahedral Zn complexes show a range of Zn–O bond distances and $10^3 \ln\beta$ $^{66}Zn/^{64}Zn$ depending on the tunnel composition, which could lead to the slightly negative isotopic fractionation observed (Table 4; Fig. 6). We note that while Zn^{2+} structures in aqueous solution and todorokite tunnels are dynamic and highly disordered, the fractionation factors reported in the current study are based on certain end-member structures; more accurate values could be obtained by exhaustive sampling for disordered Zn^{2+} configurations via MD simulations. At higher pH values from 6 to 8, a mixture of outer-sphere octahedral and inner-sphere tetrahedral Zn occurs, and Zn isotopic compositions of the adsorbed phase become heavier than the aqueous phase as pH increases (Fig. 4c). EXAFS is unable to discern a change in coordination numbers when there is a mix of two similarly coordinated complexes (i.e., four coordination and six coordination), and while there is likely to be a small decrease in the average coordination number of the combined complexes (Table 3), this cannot be resolved with EXAFS because the uncertainty in the coordination numbers is at least ±1 (Ravel and Kelly, 2007). However, a decrease in the coordination number does occur at high pH values due to the formation of tetrahedral Zn with lower coordination numbers, and this decrease is likely responsible for the slightly positive fractionation ($\Delta^{66}Zn_{adsorbed\text{-}aqueous} \sim 0.05 \pm 0.05‰$) (Fig. 8). On the other hand, interatomic distances have also often been used to rationalize isotopic fractionation trends (Guinoiseau et al., 2016; Nelson et al., 2017), where essentially heavy Zn isotopes are found to be more likely enriched in structures with low interatomic distances in which Zn has stiffer bonds (Schauble, 2004). However, it should be noted that coordination is often correlated to bond distances that a structure with lower coordination numbers would be associated with shorter bond length (Juillot et al., 2008). According to a comparison of our calculated vibrational frequencies (Fig. S3), todorokite with tetrahedral Zn tends to exhibit higher vibrational frequencies related to Zn–O bonds than todorokite with octahedral Zn, although H_2O vibrational modes are also involved in the frequencies. The current DFT calculation predicts that the equilibrium fractionation factor between inner-sphere tetrahedral Zn on todorokite and aqueous Zn ranges from 0.5–0.8 ‰ at 300 K (Table 4), similar to the experimental fractionation values for tetrahedral Zn adsorbed on the surface of silica (Nelson et al., 2017), ferrihydrite (Juillot et al., 2008), Al oxide (Gou et al., 2018), and kaolinite (Guinoiseau et al., 2016). This does indicate that tetrahedral Zn on todorokite concentrates heavy isotopes, and thus, the presence of tetrahedral Zn at high pH values

(e.g., pH 8) could explain our experimental observations that Zn isotopic fractionation ($\Delta^{66}Zn_{adsorbed-aqueous}$) evolves from –0.1 ± 0.04‰ at pH 3 with only outer-sphere octahedral complexes to 0.05 ± 0.05‰ at pH 8 with a mixture of outer-sphere octahedral complexes and inner-sphere tetrahedral complexes. Overall, the isotopic fractionation of Zn during adsorption to todorokite is driven by Zn speciation changes after adsorption versus its aqueous form before adsorption. The formation of outer-sphere octahedral surface complexes that have a long Zn-O distance close to the structure of the aqueous $Zn(H_2O)_6^{2+}$ cluster results in insignificant Zn isotope fractionation, whereas the formation of inner-sphere tetrahedral surface complexes yields a shorter Zn-O distance than the aqueous $Zn(H_2O)_6^{2+}$ cluster enriches heavier isotopes (Fig. 6).

4.3 Implications for understanding Zn isotope signatures in Mn-rich marine sediments

To date, previous work has measured the Zn isotope signatures of natural Fe-Mn crusts and nodules, which contain birnessite-type Mn oxides, and the relationship between Zn adsorption and isotopic fractionation for birnessite in controlled experiments. Work shows that natural Fe–Mn crusts and nodules are enriched in heavy Zn isotopes relative to seawater (~0.5‰) (Marechal et al., 2000; Bermin et al., 2006; Conway et al., 2013; Little et al., 2014a; Zhao et al., 2014), while birnessite at high ionic strength (i.e., synthetic seawater solutions), which is analogous to birnessite in Fe-Mn deposits, is also enriched in heavy Zn isotopes (Bryan et al., 2015). The surface layers of Fe–Mn nodules from different oceanic areas are also enriched in heavy Zn isotopes relative to seawater but have variable Zn isotope compositions, ranging from 0.53‰ to 1.16‰ (Marechal et al., 2000), while the Zn isotope compositions of a depth profile from three Fe-Mn crusts also vary between 0.8‰ and 1.2‰ (Little et al., 2014a). In the experimental work above (Bryan et al., 2015), a Zn isotopic fractionation ($\Delta^{66}Zn_{adsorbed-solution}$) of 2.74‰ is reported at low surface loadings, which is reduced to 0.16‰ for high surface loadings. The observations that Fe-Mn deposits concentrate heavy Zn isotopes with a range of isotopic compositions (Marechal et al., 2000; Little et al., 2014a) therefore appear to be explained by the presence of birnessite in natural Fe-Mn crusts and nodules with variable surface loadings of adsorbed Zn. To understand how Zn adsorption drives Zn isotopic fractionation, previous work also employs X–ray fluorescence mapping of Fe-Mn crusts to confirm that Zn is predominantly associated with birnessite and EXAFS spectroscopy to show that Zn exists in tetrahedral coordination in these deposits (Little et al., 2014b).

The enrichment of Fe-Mn crusts in heavier Zn isotopes and of oxic marine sediments that contain birnessite-type Mn oxides is thus attributed to the adsorption of Zn via tetrahedral complexes at the birnessite surface, which enrich heavy Zn isotopes (Little et al., 2014b; Bryan et al., 2015).

Todorokite is one of the main Mn-bearing phases in oxic marine sediments, where it is typically intimately associated with birnessite-type minerals (Burns and Burns, 1977; Post, 1999; Peacock and Moon, 2012). It is thought to only form as a result of the aging and associated mineralogical transformation of birnessite (Feng et al., 2004; Atkins et al., 2014), and todorokite is especially present in diagenetic settings and low-temperature hydrothermal settings, where the transformation of birnessite-type precursor phases is favored (Burns and Burns, 1977). For example, todorokite is rarely found in hydrogenetic ferromanganese crusts precipitated directly from ambient seawater (authigenic) where birnessite-type minerals are dominant but is found in variable proportions in diagenetic ferromanganese nodules formed at the sediment–seawater interface, reflecting the influence of sediment pore waters on individual nodules, and it is prevalent below the sediment–seawater interface in close proximity to hydrothermal fluids (Burns and Burns, 1977; Post, 1999). In the present study, we quantify Zn isotope fractionation during adsorption to todorokite for the first time. The results show that the magnitude of Zn isotopic fractionation during adsorption to todorokite is much smaller than that measured above for Zn isotope signatures in Fe-Mn crusts and nodules (Table 2). It is true that the isotopic composition of Zn adsorbed to todorokite becomes heavier from pH 3 to 8 (Fig. 4), as the Zn complexes evolve from outer-sphere octahedral coordination to a mixture of outer-sphere octahedral and inner-sphere tetrahedral coordination, but the isotopic fractionation ($\Delta^{66}Zn_{adsorbed-solution}$ = 0.05 ± 0.05‰) at circumneutral pH is still very small compared to the average $\Delta^{66}Zn_{Mn\ oxides-seawater}$ value of ~0.5‰ (Marechal et al., 2000; Bermin et al., 2006; Little et al., 2014a; Zhao et al., 2014). Furthermore, while our DFT calculations predict equilibrium fractionation between pure inner-sphere tetrahedral Zn on todorokite and aqueous Zn to range from 0.5–0.8‰, it is unlikely that pure tetrahedral Zn exists at the Zn/Mn atomic ratio (~0.004) of natural Mn-rich marine sediments (Manheim and Lane-Bostwick, 1991) (Fig. S2). Instead, isotopic fractionation between todorokite and solution close to natural conditions should approach –0.10 ± 0.04‰ (Fig. S2).

Further work is needed to determine the extent to which the Zn isotopic fractionation values determined in this work are directly applicable to natural marine sediments. Our experimental

conditions of circumneutral pH are close to the pH of marine sediment porewaters (Reimers et al., 1996), and while our experiments differ in terms of temperature and ionic strength compared to marine sediment porewaters, this is not expected to substantially alter Zn adsorption or isotopic fractionation behavior. Specifically, the slightly elevated temperature used here compared to typical marine sediment porewaters (~10 °C) is unlikely to substantially change Zn adsorption or isotopic fractionation behavior (Fujii et al., 2010; Ducher et al., 2016). Additionally, the elevated temperature used here to more rapidly induce the transformation of birnessite to todorokite than occurs in marine sediments is shown not to result in a different transformation mechanism or pathway for birnessite to todorokite and is thus not expected to alter the mechanism of Zn adsorption or isotopic fractionation (Atkins et al., 2014, 2016). The ionic strength of our experimental system is lower than that in marine sediment porewaters, but for Zn inorganic speciation, the dominant species of Zn in porewaters is expected to be Zn^{2+}(aq) (Byrne, 2002) and thus the same as that in our experimental system. Our experimental conditions of ionic speciation potentially differ compared to marine sediment porewaters, however, in terms of Zn organic speciation. Organic ligands in marine sediments can chelate trace metals such as Zn and may induce associated isotopic fractionation (Jouvin et al., 2009). Moreover, although the fate of Zn adsorbed by birnessite is likely to be ultimately controlled by its adsorption to todorokite (Atkins et al., 2016; Little et al., 2020), the isotopic behavior of Zn during its migration from birnessite as it transforms into todorokite and its subsequent adsorption to todorokite may not be completely captured in our experiments that do not include the transformation process. Therefore, the exact isotopic compositions of Zn in marine todorokite might be hard to predict. Overall, however, we suggest that Zn isotopic fractionation in natural marine todorokite can be inferred from structural differences that occur between (higher coordination numbers, longer average Zn-O distance) outer-sphere octahedral complexes (thus light) and (lower coordination numbers, shorter average Zn-O distance) inner-sphere tetrahedral complexes (thus heavy). As such, we can reasonably infer that relatively light Zn isotopes are enriched in natural todorokite compared to those in natural birnessite, according to the dominant outer-sphere octahedral Zn complexes on todorokite versus inner-sphere tetrahedral Zn complexes on natural birnessite. This means that diagenetic sediments that contain todorokite are likely to be lighter than the Fe-Mn deposits and oxic sediments measured above, which are all either largely hydrogenetic (Fe-Mn crusts) or with limited diagenetic influence (surfaces of Fe-Mn nodules) or oxic/authigenic samples.

It is commonly accepted that todorokite only forms from the transformation of birnessite precursors (Burns and Burns, 1977, Feng et al., 2004; Bodei et al., 2007; Atkins et al., 2014). During this transformation process, previous work shows that Ni adsorbed by birnessite is released to solution (Atkins et al., 2016), while Co is retained in the newly formed todorokite phase (Wu et al., 2019). More generally, these studies propose that non-Jahn–Teller distorted cations, such as Ni, are released during transformation, while Jahn-Teller distorted cations, such as Co, are structurally incorporated during transformation (Atkins et al., 2014, 2016; Wu et al., 2019), and the presence of Jahn–Teller distorted trace metals could facilitate the formation of todorokite (Bodei et al., 2007; Cui et al., 2008; Atkins et al., 2014; Zhao et al., 2015). With relevance to our work, Zn, similar to Ni, does not have Jahn–Teller distortion and is thus predicted to be released to solution during the birnessite to todorokite transformation (Atkins et al., 2014, 2016). Diagenetic/suboxic sediments are thus expected to be a source of Zn to porewaters, which might potentially diffuse into the overlying water column (Aktins et al., 2014, 2016). As such, because Zn is potentially released to the water column during the transformation of birnessite to todorokite and because light Zn isotopes are enriched with todorokite compared to Zn with birnessite, it is therefore likely that these processes act in combination to result in Zn isotope compositions of diagenetic/suboxic sediments that are lighter than oxic sediments that contain authigenic Mn oxides or those with limited diagenetic influence.

Future work should investigate the Zn isotopic composition of natural sediments to help support the experimental implication that diagenetic/suboxic sediments are enriched in light Zn isotopes. The possibility of further Zn isotopic fractionation during mineralogical transformation and Zn release, which affects the isotopic signal of diagenetic/suboxic sediments, should also be investigated in controlled laboratory experiments. Finally, follow-up work should constrain the effect of organic ligands on Zn isotopic fractionation during adsorption to todorokite to ensure that experiments capture both the inorganic and organic speciation of Zn complexes in seawater.

5. Conclusion

We report the first study to quantify Zn isotope fractionation during adsorption to synthetic todorokite and constrain the fractionation mechanisms for different experimental conditions. The results

show that the molecular-level characteristics of Zn adsorption complexes can explain distinct Zn isotope signatures. Zn adsorbs to the todorokite surface at low pH as an outer-sphere octahedral complex (R_{Zn-O} = 2.06 Å) with slightly negative isotopic fractionation from aqueous Zn ($\Delta^{66}Zn_{adsorbed-aqueous}$ = –0.1 ± 0.04‰). At higher pH values, Zn begins to form a mixture of outer-sphere octahedral and inner-sphere tetrahedral complexes (R_{Zn-O} = 2.00 – 2.05 Å) at the todorokite surface with a measured equilibrium isotope fractionation ($\Delta^{66}Zn_{adsorbed-aqueous}$) ranging from –0.1 ± 0.04‰ to 0.05 ± 0.05‰. We assert that structural changes (e.g., coordination and bond distance) are the cause of the differences in Zn isotope partitioning to the todorokite surface because inner-sphere tetrahedral Zn formation on the todorokite surface with a lower coordination number and shorter Zn-O bond distance relative to outer-sphere octahedral Zn corresponds to a higher vibrational frequency and enriches heavy isotopes. Furthermore, we can constrain two distinct Zn isotopic fractionation magnitudes from DFT calculations: $\Delta^{66}Zn_{adsorbed-aqueous}$ = –0.10 ± 0.04‰ for the octahedral surface complex and $\Delta^{66}Zn_{adsorbed-aqueous}$ = 0.5–0.8 ‰ for the tetrahedral inner-sphere corner-sharing surface complex on todorokite.

The results reported here provide important new constraints for understanding Zn isotope signatures in Mn-rich marine sediments. We propose that because light Zn isotopes are enriched in todorokite compared to birnessite, diagenetic/suboxic sediments that contain todorokite as a result of the diagenetic transformation of birnessite will have lighter Zn isotope signatures than hydrogenetic Fe-Mn crusts and oxic sediments. In addition, previous work shows that Zn is expected to be released from newly formed todorokite to sediment porewater and potentially the overlying water column (Atkins et al., 2014, 2016); thus, the enrichment of light isotopes on todorokite and the release of Zn from this mineral phase might act in combination to constrain the isotope signatures of diagenetic/suboxic sediments to relatively light values. Overall, we predict that diagenetic/suboxic sediments that contain todorokite are likely enriched in lighter Zn isotopes than authigenic/oxic sediments that contain birnessite (Marechal et al., 2000; Little et al., 2014a; Bryan et al. 2015). Field studies are needed to support this experimentally based prediction, leading to a more complete understanding of Zn isotope systematics in the ocean.

Acknowledgments

We appreciate the constructive comments from the AE, Prof. Brandy Toner, and three anonymous reviewers, which greatly improved this manuscript. This research was funded by the National Natural Science Foundation of China (NSFC) (Grant Nos. 41977267, 41722303). Kideok Kwon was supported by the Basic Science Research Program of the National Research Foundation of Korea (NRF) (2019R1A2C2084299). Wei Li and Caroline Peacock are grateful to the international collaborative research funding from the National Natural Science Foundation of China (NSFC) (Grant No. 42011530177) and the Royal Society Newton Mobility Grant (IEC/NSFC/191423). Wei Li is grateful for the financial support for the Fundamental Research Funds for the Central Universities, Nanjing University, and the support from the Chinese Academy of Sciences' State Key Laboratory of Environment Geochemistry (SKLEG2019712). EXAFS data collection was carried out with the assistance of Drs. Jing Zhang and Lirong Zheng at the 1W1B beamline of Beijing Synchrotron Radiation Facility (BSRF) operated by Chinese Academy of Sciences.

References

Arrhenius G. (1963) Pelagic sediments. In *Sea, 3* (ed. M. N. Hill) Interscience, New York, pp. 655–727.

Ackland, G. J., Warren, M. C. and Clark, S. J. (1997) Practical methods in *ab initio* lattice dynamics. *J. Phys. Condens. Matter*. **9**, 7861.

Allison J. D., Brown D. S. and Novo-Gradac K. J. (1991) MINTEQA2/PRODEFA2, A geochemical assessment model for environmental systems. U.S. Environmental Protection Agency. Report No. EPA/600/3-91/021.

Atkins A. L., Shaw S. and Peacock C. L. (2014) Nucleation and growth of todorokite from birnessite: implications for trace metal cycling in marine sediments. *Geochim. Cosmochim. Acta* **144**, 109–125.

Atkins A. L., Shaw S. and Peacock C. L. (2016) Release of Ni from birnessite during transformation of birnessite to todorokite: implications for Ni cycling in marine sediments. *Geochim. Cosmochim. Acta* **189**, 158–183.

Balistrieri L. S., Borrok D. M., Wanty R. B. and Ridley W. I. (2008) Fractionation of Cu and Zn isotopes during adsorption onto amorphous Fe(III) oxyhydroxide: experimental mixing of acid rock

drainage and ambient river water. *Geochim. Cosmochim. Acta* **72**, 311–328.

Barling J. and Anbar A. D. (2004) Molybdenum isotope fractionation during adsorption by manganese oxides. *Earth Planet. Sci. Lett*. **217**, 315–329.Bermin J., Vance D., Archer C. and Statham P. J. (2006) The determination of the isotopic composition of Cu and Zn in seawater. *Chem. Geol*. **226**, 280–297.

Bigeleisen J. and Mayer M. G. (1947) Calculation of equilibrium constants for isotopic exchange reactions. *J. Chem. Phys.* **15**, 261–267.

Blanchard, M., Balan, E. and Schauble, E. A. (2017) Equilibrium fractionation of non-traditional isotopes: A Molecular Modeling Perspective, in: Teng, F.-Z., Watkins, J.M., Dauphas, N. (Eds.), *Rev Mineral Geochem*, pp. 27-63.

Bochatay, L., and Persson, P. (2000). Metal ion coordination at the watermanganite (gamma MnOOH) interface II. An EXAFS study of zinc(II). *J. Coll. Interf. Sci*. **229**, 593–599.

Bodei S., Manceau A., Geoffroy N., Baronnet A. and Buatier M. (2007) Formation of todorokite from vernadite in Ni-rich hemipelagic sediments. *Geochim. Cosmochim. Acta* **71**, 5698–5716.

Bryan A. L., Dong S., Wilkes E. B. and Wasylenki L. E. (2015) Zinc isotope fractionation during adsorption onto Mn oxyhydroxide at low and high ionic strength. *Geochim. Cosmochim. Acta* **157**, 182–197.

Burns R. G. and Burns V. M. (1977) Mineralogy of ferromanganese nodules. In *Marine Manganese Deposits* (ed. G. P. Glasby). Elsevier, Amsterdam.

Burns R. G., Burns V. M. and Stockman H. W. (1983) A review of the todorokite-buserite problem: implications to the mineralogy of marine manganese nodules. *Am. Mineral.* **68**, 972–980.

Burns R. G., Burns V. M. and Stockman H. W. (1985) The todorokite-buserite problem: further considerations. *Am. Mineral*. **70**, 205–208.

Byrne R. H. (2002) Inorganic speciation of dissolved elements in seawater: the influence of pH on concentration ratios. *Geochem. Trans.* **3**, 11–16.

Cismasu A. C., Levard C. M., Michel F. M. and Brown G. E. (2013) Properties of impurity-bearing ferrihydrite II. Insights into the surface composition of Al- and Si-bearing ferrihydrite from Zn(II) sorption experiments and Zn K-edge X-ray absorption spectroscopy. *Geochim. Cosmochim. Acta* **119**, 46–60.

Clark, S. J., Segall, M. D., Pickard, C. J., Hasnip, P. J., Probert, M. J., Refson, K. and Payne, M. C. (2005) First principles methods using CASTEP. *Zeitschrift für Krist.* **220**, 567–570.

Conway T. M., Rosenberg A. D., Adkins J. F. and John S. G. (2013) A new method for precise determination of iron, zinc and cadmium stable isotope ratios in seawater by double-spike mass spectrometry. *Anal. Chim. Acta* **793**, 44–52.

Conway T. M., John S. G. (2014) The biogeochemical cycling of zinc and zinc isotopes in the North Atlantic Ocean. *Glob. Biogeochem. Cycles* **28**, 1111–1128.

Conway T. M., John S. G. (2015) The cycling of iron, zinc and cadmium in the North East Pacific Ocean – insights from stable isotopes. *Geochim. Cosmochim. Acta* **164**, 262–283.

Dong S. and Wasylenki L. E. (2016) Zinc isotope fractionation during adsorption to calcite at high and low ionic strength. *Chem. Geol.* **447**, 70–78.

Ducher M., Blanchard M. and Balan E. (2016) Equilibrium zinc isotope fractionation in Zn-bearing minerals from first-principles calculations. *Chem. Geol.* **443**, 87–96.

Ducher, M., Blanchard, M. and Balan, E. (2018) Equilibrium isotopic fractionation between aqueous Zn and minerals from first-principles calculations. *Chem. Geol*. **483**, 342-350.

Elzinga E. J. and Reeder R. J. (2002) X-ray absorption spectroscopy study of Cu^{2+} and Zn^{2+} adsorption complexes at the calcite surface: Implications for site-specific metal incorporation preferences during calcite crystal growth. *Geochim. Cosmochim. Acta* **22**, 3943–3954.

Feng X. H., Tan W. F., Liu F., Wang J. B. and Ruan H. D. (2004) Synthesis of todorokite at atmospheric pressure. *Chem. Mater.* **16**, 4330–4336.

Feng X., Zhu M., Ginder-Vogel M., Ni C., Parikh S. and Sparks D. (2010) Formation of nano-crystalline todorokite from biogenic Mn oxides. *Geochim. Cosmochim. Acta* **74**, 3232–3245.

Fujii T., Moynier F., Telouk P. and Abe M. (2010) Experimental and theoretical investigation of isotope fractionation of zinc between aqua, chloro, and macrocyclic complexes. *J. Phys. Chem.* **114**, 2543–2552.

Fujii T., Moynier F., Blichert-Toft J. and Albarede F. (2014) Density functional theory estimation of isotope fractionation of Fe, Ni, Cu, and Zn among species relevant to geochemical and biological environments. *Geochim. Cosmochim. Acta* **140**, 553–576

Ghose, S. (1964) The crystal structure of hydrozincite, $Zn_5(OH)_6(CO_3)_2$. *Acta Crystallogr*. **17**, 1051-

1057.

Gou W., Li W., Ji J. F. and Li W. (2018) Zinc isotope fractionation during sorption onto Al oxide: atomic level understanding from EXAFS. *Environ. Sci. Technol.* **52**, 9087-9096.

Gräfe M. and Sparks D. L. (2005) Kinetics of zinc and arsenate co-sorption at the goethite–water interface. *Geochim. Cosmochim. Acta* **69**, 4573-4595.

Guinoiseau D., Gelabert A., Moureau J., Louvat P. and Benedetti M. F. (2016) Zn isotope fractionation during sorption onto kaolinite. *Environ. Sci. Technol.* **50**, 1844–1852.

Isson T. T., Love G. D., Dupont C. L., Reinhard C. T., Zumberge A. J., Asael D., Gueguen B., McCrow J., Gill B. C., Owens J., Rainbird R. H., Rooney A. D., Zhao M. Y., Stueeken E. E., Konhauser K. O., John S. G., Lyons T. W. and Planavsky N. J. (2018) Tracking the rise of eukaryotes to ecological dominance with zinc isotopes. *Geobiology* **16**, 341–352.

John S. G. and Conway T. M. (2014) A role for scavenging in the marine biogeochemical cycling of zinc and zinc isotopes. *Earth Planet. Sci. Lett.* **394**, 159–167.

Jouvin D., Louvat P., Juillot F., Maréchal C. N. and Benedetti M. F. (2009) Zinc isotopic fractionation: why organic matters. *Environ. Sci. Technol.* **43**, 5747–5754

Juillot F., Marechal C., Ponthieu M., Cacaly S., Morin G., Benedetti M., Hazemann J. L., Proux O. and Guyot F. (2008) Zn isotopic fractionation caused by sorption on goethite and 2-lines ferrihydrite. *Geochim. Cosmochim. Acta* **72**, 4886–4900.

Kaltak, M., Fernández-Serra, M. and Hybertsen, M. S. (2017) Charge localization and ordering in $A_2Mn_8O_{16}$ hollandite group oxides: Impact of density functional theory approaches. *Phys. Rev. Materials* **1**, 075401.

Koschinsky A. and Halbach P. (1995) Sequential leaching of marine ferromanganese precipitates: genetic implications. *Geochim. Cosmochim. Acta* **59**, 5113–5132.

Koschinsky A. and Hein J. R. (2003) Uptake of elements from seawater by ferromanganese crusts: solid-phase associations and seawater speciation. *Mar. Geol.* **198**, 331–351.

Little S. H., Vance D., Walker-Brown C. and Landing W. M. (2014a) The oceanic mass balance of copper and zinc isotopes, investigated by analysis of their inputs, and outputs to ferromanganese oxide sediments. *Geochim. Cosmochim. Acta* **125**, 673–693.

Little S. H., Sherman D. M., Vance D. and Hein J. R. (2014b) Molecular controls on Cu and Zn isotopic

fractionation in Fe–Mn crusts. *Earth Planet. Sci. Lett.* **396**, 213–222.

Little S. H., Vance D., McManus J. and Severmann S. (2016) Key role of continental margin sediments in the oceanic mass balance of Zn and Zn isotopes. *Geology* **44**, 207–210.

Little S. H., Archer C., McManus J., Najorka J., Wegorzewski A. V. and Vance D. (2020) Towards balancing the oceanic Ni budget. *Earth Planet. Sci. Lett.* **547**, 116461.

Liu S. A., Liu P. P., Lv Y., Wang Z. Z. and Dai J. G. (2019) Cu and Zn isotope fractionation during oceanic alteration: implications for Oceanic Cu and Zn cycles. *Geochim. Cosmochim. Acta* **257**, 191-205.

Manceau A., Lanson B. and Drits V. A. (2002) Structure of heavy metal sorbed birnessite: part III. Results from powder and polarized extended X-ray absorption fine structure spectroscopy. *Geochim. Cosmochim. Acta* **66**, 2639–2663.

Manceau A., Lanson M. and Geoffroy N. (2007) Natural speciation of Ni, Zn, Ba and As in ferromanganese coatings on quartz using X-ray fluorescence, absorption and diffraction. *Geochim. Cosmochim. Acta* **71**, 95–128.

Manheim F. and Lane-Bostwick C. (1991) Chemical composition of ferromanganese crusts in the world ocean: a review and comprehensive chemical composition of ferromanganese crusts in the world ocean: a review and comprehensive database. *Open-File Report* 89–020, U.S. Geological Survey, Woods Hole, MA.

Marechal C. N., Telouk P. and Albarede F. (1999) Precise analysis of copper and zinc isotopic compositions by plasma-source mass spectrometry. *Chem. Geol.* **156**, 251–273.

Marechal C., Nicolas E., Douchet C. and Albarede F. (2000) Abundance of zinc isotopes as a marine biogeochemical tracer. *Geochem. Geophys. Geosyst.* **1**, 1015.

Markovic, T., Manzoor, S., Humphreys-Williams, E., Kirk, G. J. D., Vilar, R. and Weiss, D. J. (2017) Experimental determination of zinc isotope fractionation in complexes with the phytosiderophore 2′-deoxymugeneic Acid (DMA) and its structural analogues, and implications for plant uptake mechanisms. *Environ. Sci. Technol.* **51**, 98–107.

McKenzie R. M. (1971) The synthesis of birnessite, cryptomelane, and some other oxides and hydroxides of manganese. *Mineral. Mag.* **38**, 493–503.

Momma, K. and Izumi, F. (2011) VESTA 3 for three-dimensional visualization of crystal, volumetric and morphology data. *J. Appl. Crystallogr*. **44**, 1272–1276.

Monkhorst, H. and Pack, J. (1976) Special points for Brillouin zone integrations. *Phys. Rev. B* **13**, 5188–5192.

Moore C. M., Mills M. M., Arrigo K. R., Berman-Frank I., Bopp L., Boyd P. W., Galbraith E. D., Geider R. J., Guieu C., Jaccard S. L., Jickells T. D., La Roche J., Lenton T. M., Mahowald N. M., Marañón E., Marinov I., Moore J. K., Nakatsuka T., Oschlies A., Saito M. A., Thingstad T. F., Tsuda A. and Ulloa O. (2013) Processes and patterns of oceanic nutrient limitation. *Nat. Geosci.* **6**, 701–710.

Morel F. M., Reinfelder J. R., Chamberlain C. P., Roberts S. B., Lee J. G. and Yee D. (1994) Zinc and carbon co-limitation of marine phytoplankton. *Nature* **369**, 740–742.

Moynier F., Vance D., Fujii T. and Savage P. (2017) The isotope geochemistry of zinc and copper. *Rev. Mineral. Geochem*. **82**, 543–600.

Nachtegaal M. and Sparks D. L. (2004) Effect of iron oxide coatings on zinc sorption mechanisms at the clay-mineral/water interface. *J. Colloid Interface Sci.* **276**, 13–23.

Nakada R., Tanaka M., Tanimizu M. and Takahashi Y. (2017) Aqueous speciation is likely to control the stable isotopic fractionation of cerium at varying pH. *Geochim. Cosmochim. Acta* **218**, 273-290.

Nelson J., Wasylenki L., Bargar J. R., Brown G. E. and Maher K. (2017) Effects of surface structural disorder and surface coverage on isotopic fractionation during Zn(II) adsorption onto quartz and amorphous silica surfaces. *Geochim. Cosmochim. Acta* **215**, 354-376.

Parlinski, K., Li, Z.Q. and Kawazoe, Y. (1997) First-principles determination of the soft mode in cubic ZrO_2. *Phys. Rev. Lett*. **78**, 4063–4066.

Pavlov M., Siegbahn P. E. and Sandström M. (1998) Hydration of beryllium, magnesium, calcium, and zinc ions using density functional theory. *J. Phys. Chem. A* **102**, 219-228.

Peacock C. L. and Moon E. M. (2012) Oxidative scavenging of thallium by birnessite: explanation for thallium enrichment and stable isotope fractionation in marine ferromanganese precipitates. *Geochim. Cosmochim. Acta* **84**, 297–313.

Perdew, J., Burke, K. and Ernzerhof, M. (1996) Generalized Gradient Approximation Made Simple. *Phys. Rev. Lett***. 77**, 3865–3868.

Pokrovsky O. S., Viers J. and Freydier R. (2005) Zinc stable isotope fractionation during its adsorption on oxides and hydroxides. *J. Colloid Interface Sci.* **291**, 192–200.

Post J. E. and Appleman D. E. (1988) Chalcophanite, $ZnMn_3O_7$ $3H_2O$: New crystal-structure determinations. *Am. Mineral*. **73**, 1401–1404.

Post J. E. (1999) Manganese oxide minerals: crystal structures and economic and environmental significance. *Proc. Natl. Acad. Sci. U. S. A.* **96**, 3447–3454

Post J. E., Heaney P. J. and Hanson J. (2003) Synchrotron X-ray diffraction study of the structure and dehydration behavior of todorokite. *Am. Mineral.* **88**, 142–150.

Pye C. C., Corbeil C. R. and Rudolph W. W. (2006) An ab initio investigation of zinc chloro complexes. *Phys. Chem. Chem. Phys*. **8**, 5428–5436.

Ravel B. and Kelly S. D. (2007) The difficult chore of measuring coordination by EXAFS. In: *X-Ray Absorption Fine Structure–XAFS* **13**, pp. 150–152.

Reimers C. E., Ruttenberg K. C., Canfield D. E., Christiansen M. B. and Martin J. B. (1996) Porewater pH and authigenic phases formed in the uppermost sediments of the Santa Barbara basin. *Geochim. Cosmochim. Acta* **60**, 4037–4057.

Rosman K. J. R. and Taylor P. D. P. (1998) Isotopic compositions of the elements. *Pure Appl. Chem.* **70**, 217–235

Ryan, B. M., Kirby, J. K., Degryse, F., Scheiderich, K. and McLaughlin, M. J. (2014) Copper isotope fractionation during equilibration with natural and synthetic ligands. *Environ. Sci. Technol.* **48**, 8620–8626.

Sandstead H. H. (2014) Zinc. In: *Handbook on the Toxicology of Metals Elsevier*, pp. 1369–1386.

Schauble E. A. (2004) Applying stable isotope fractionation theory to new systems. *Rev. Mineral. Geochem.* **55**, 65–111.

Sinoir M., Butler E. C., Bowie A. R., Mongin M., Nesterenko P. N. and Hassler C. S. (2012) Zinc marine biogeochemistry in seawater: A review. *Marine & Freshwater Research*, v. **63**, p. 644–657, doi:10.1071/MF11286

Sweere T. C., Dickson A. J., Jenkyns H. C., Porcelli D., Elrick M., van den Boorn S. H. J. M. and Henderson G. M. (2018) Isotopic evidence for changes in the zinc cycle during Oceanic Anoxic Event 2 (Late Cretaceous). *Geology* **46**, 463–466.

Vance D., Little S. H., Archer C., Cameron V., Andersen M. B., Rijkenberg M. J. and Lyons T. W. (2016) The oceanic budgets of nickel and zinc isotopes: the importance of sulfidic environments as illustrated by the Black Sea. *Phil. Trans. R. Soc. A* **374**, 20150294.

Vanderbilt, D. (1990) Soft self-consistent pseudopotentials in a generalized eigenvalue formalism. *Phys. Rev. B* **41**, 7892–7895.

Wang Y., Benkaddour S., Marafatto F. F. and Peña J. (2018) Diffusion- and pH-dependent reactivity of layer-type MnO_2: Reactions at particle edges versus vacancy sites. *Environ. Sci. Technol.* **52**, 3476–3485.

Wasylenki L. E., Rolfe B. A., Weeks C. L., Spiro T. G. and Anbar A. D. (2008) Experimental investigation of the effects of temperature and ionic strength on Mo isotope fractionation during adsorption to manganese oxides. *Geochim. Cosmochim. Acta* **72**, 5997–6005.

Wasylenki L. E., Swihart J. W. and Romaniello S. J. (2014) Cadmium isotope fractionation during adsorption to Mn oxyhydroxide at low and high ionic strength. *Geochim. Cosmochim. Acta* **140**, 212–226.

Waychunas G. A., Fuller C. C. and Davis J. A. (2002) Surface complexation and precipitate geometry for aqueous Zn(II) sorption on ferrihydrite I: X-ray absorption extended fine structure spectroscopy analysis. *Geochim. Cosmochim. Acta* **66**, 1119–1137.

Wick S., Pena J. and Voegelin A. (2019) Thallium sorption onto manganese oxides. *Environ. Sci. Technol*. **53**, 13168–13178.

Wiederhold J. G. (2015) Metal stable isotope signatures as tracers in environmental geochemistry. *Environ. Sci. Technol*. **49**, 2606-2624.

Wu Z., Peacock C. L., Lanson B., Yin H., Zheng L., Chen Z., Tan W., Qiu G., Liu F. and Feng X. (2019) Transformation of containing birnessite to todorokite: Effect of Co on the transformation and implications for Co mobility. *Geochim. Cosmochim. Acta* **246**, 21–40.

Zhao Y., Vance D., Abouchami W. and de Baar H. J. W. (2014) Biogeochemical cycling of zinc and its isotopes in the Southern Ocean. *Geochim. Cosmochim. Acta* **125**, 653–672.

Figures and Tables

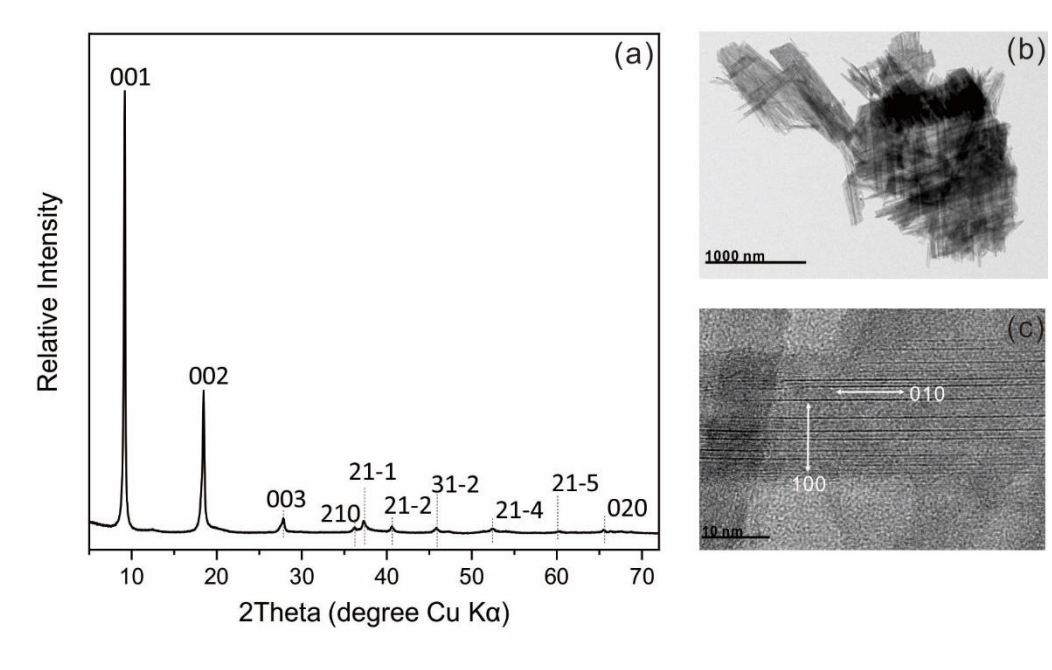

Fig. 1. Characterization of synthetic todorokite using powder X-ray diffraction (a) and transmission electron microscopy (TEM) (b, c). X-ray diffraction peaks are labeled based on JCPDS-38-0475 for todorokite. 010 and 100 in (c) indicate lattice plane directions.

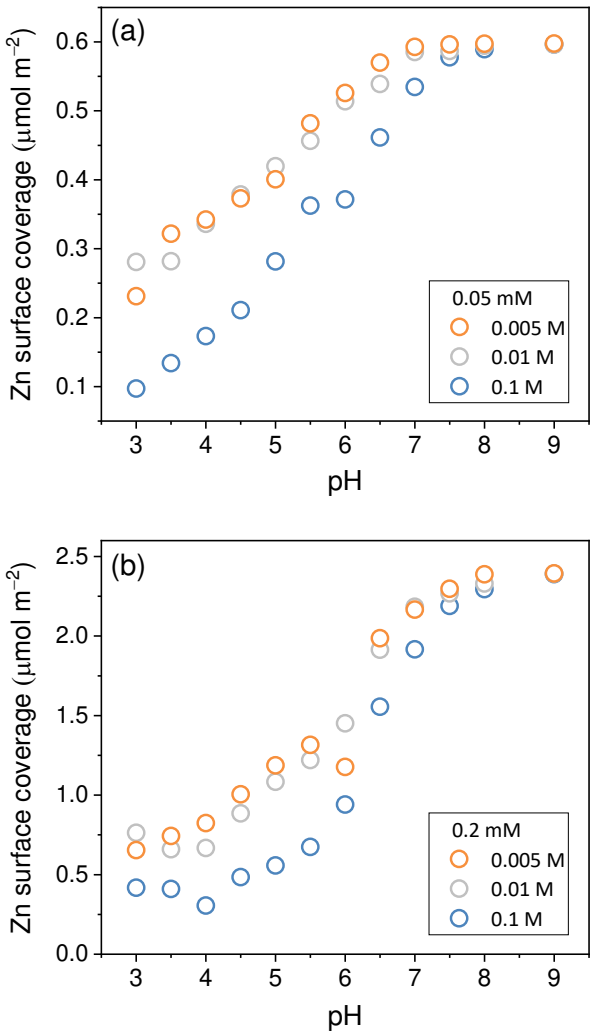

Fig. 2. Effect of pH on Zn adsorption to todorokite at different ionic strengths. Adsorption experiments were carried out at two Zn concentrations of 0.05 mM (a) and 0.2 mM (b). The solid/solution ratio was set to 0.4 g/L suspension, the equilibrium time was 48 h, and room temperature was 25 ± 1 °C.

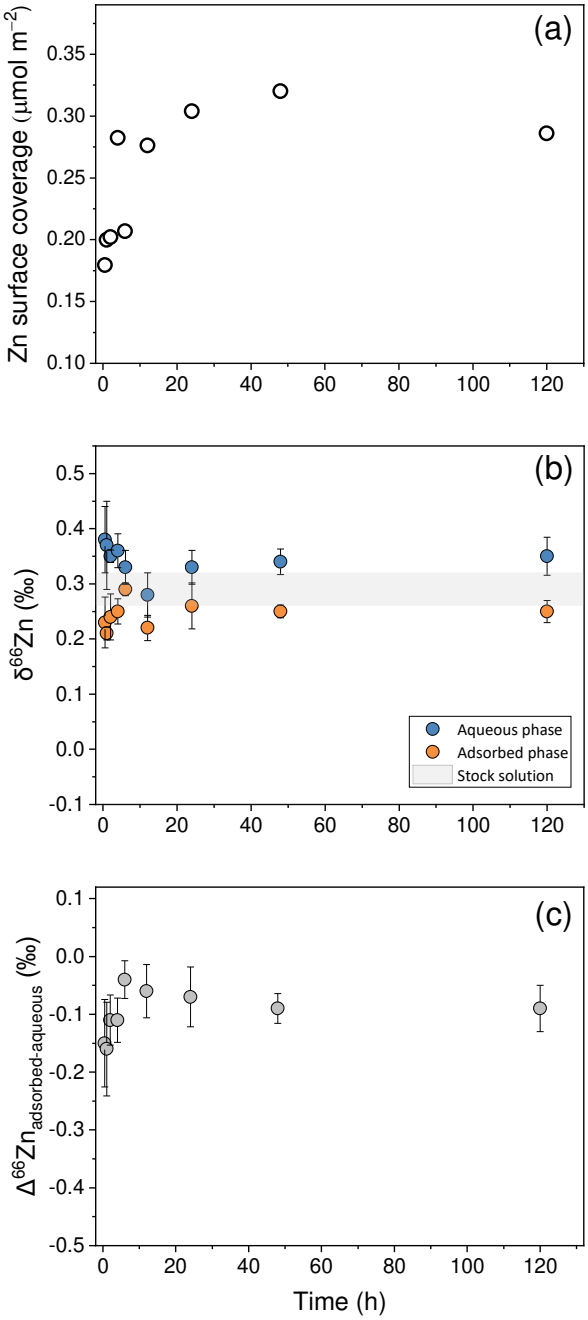

Fig. 3. Time-series experiments of (a) Zn adsorption kinetics, (b) δ^{66}Zn values for adsorbed Zn and aqueous Zn; (c) Zn stable isotopic fractionation between adsorbed Zn and aqueous Zn phases. The experiments were carried out at a Zn concentration of 0.05 mM at pH 6 in a background electrolyte of 0.1 M $NaNO_3$ at a solid/solution ratio of 0.4 g/L and room temperature (25 ± 1 °C). The gray shaded area indicates the initial Zn isotope composition of the stock solution used in all experiments. Error bars represent 2SD on 3 replicate analyses of each sample.

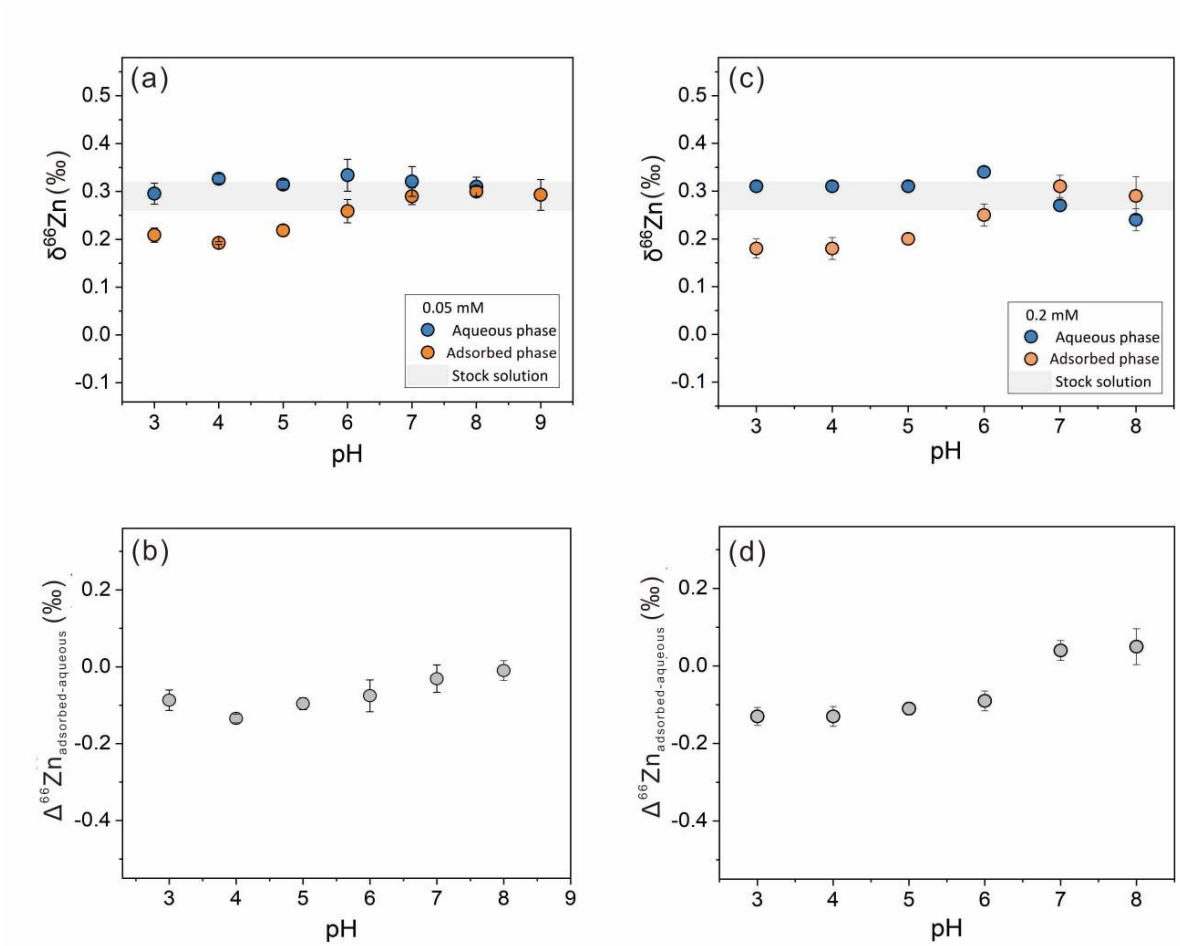

Fig. 4. Plots of Zn isotope compositions of adsorbed Zn and aqueous Zn and Zn isotopic fractionation between the two phases in adsorption edge experiments at 0.05 mM Zn loading (a, b) and adsorption edge experiments at 0.2 mM Zn loading (c, d). The gray shaded area indicates the initial Zn isotope composition of the stock solution used in all experiments. Error bars represent 2SD on 3 replicate analyses of each sample.

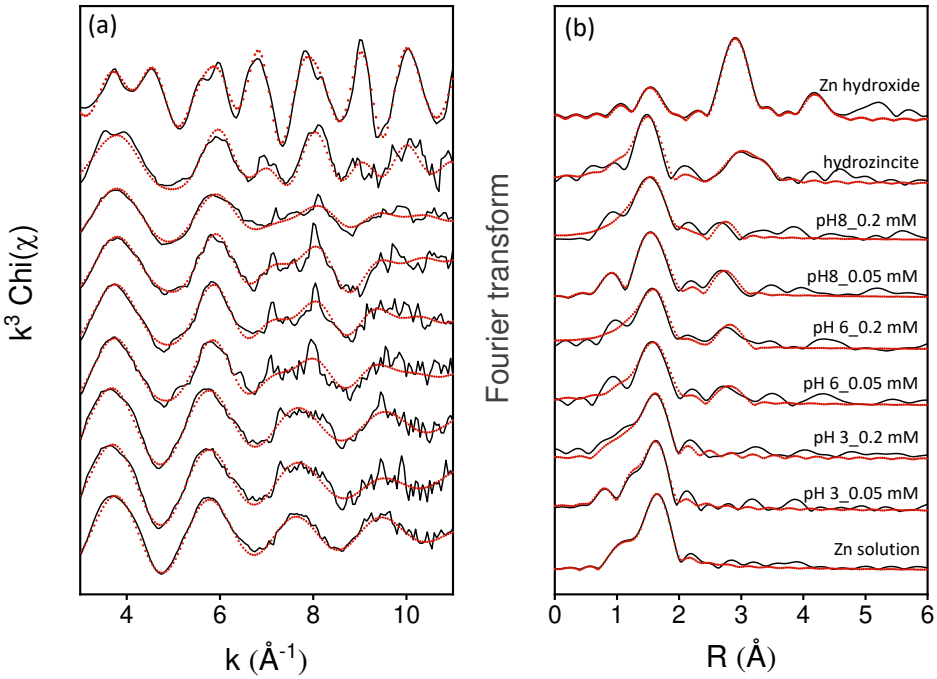

Fig. 5. (a) k^3-weighted Zn *K*-edge EXAFS data of Zn adsorption samples and reference compounds; (b) corresponding Fourier transforms in R space. Experimental and shell-by-shell fitting data are shown as black solid lines and red dots, respectively.

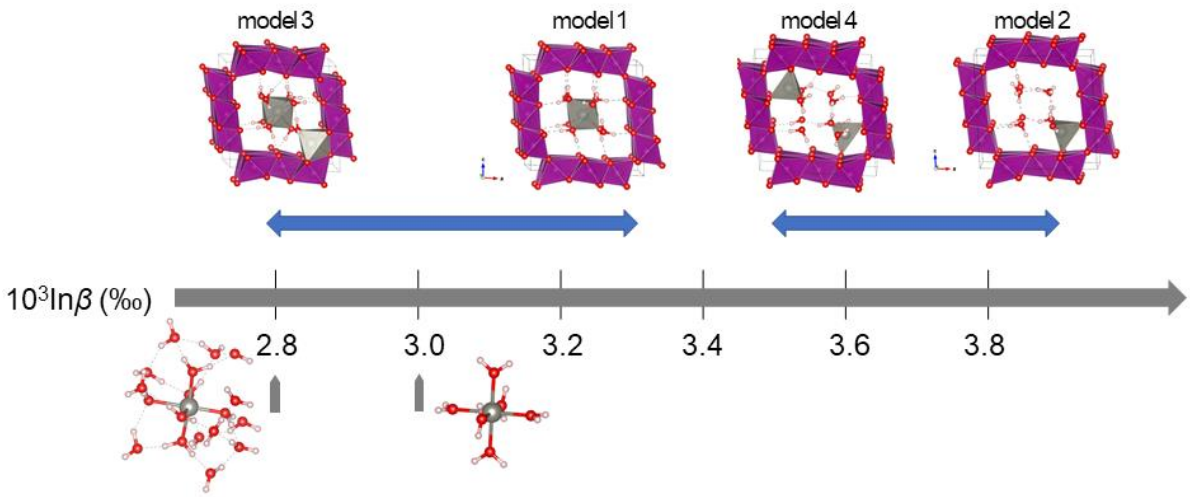

Fig. 6. A range of beta factors ($10^3 \ln\beta\ ^{66}Zn/^{64}Zn$) DFT-calculated at 300 K for aqueous Zn^{2+} clusters and Zn-todorokite adsorption models (models 1–4). Purple octahedron = Mn octahedron; gray polyhedra = Zn octahedra or tetrahedra; red = O; pink = H; dashed lines = H-bonds.

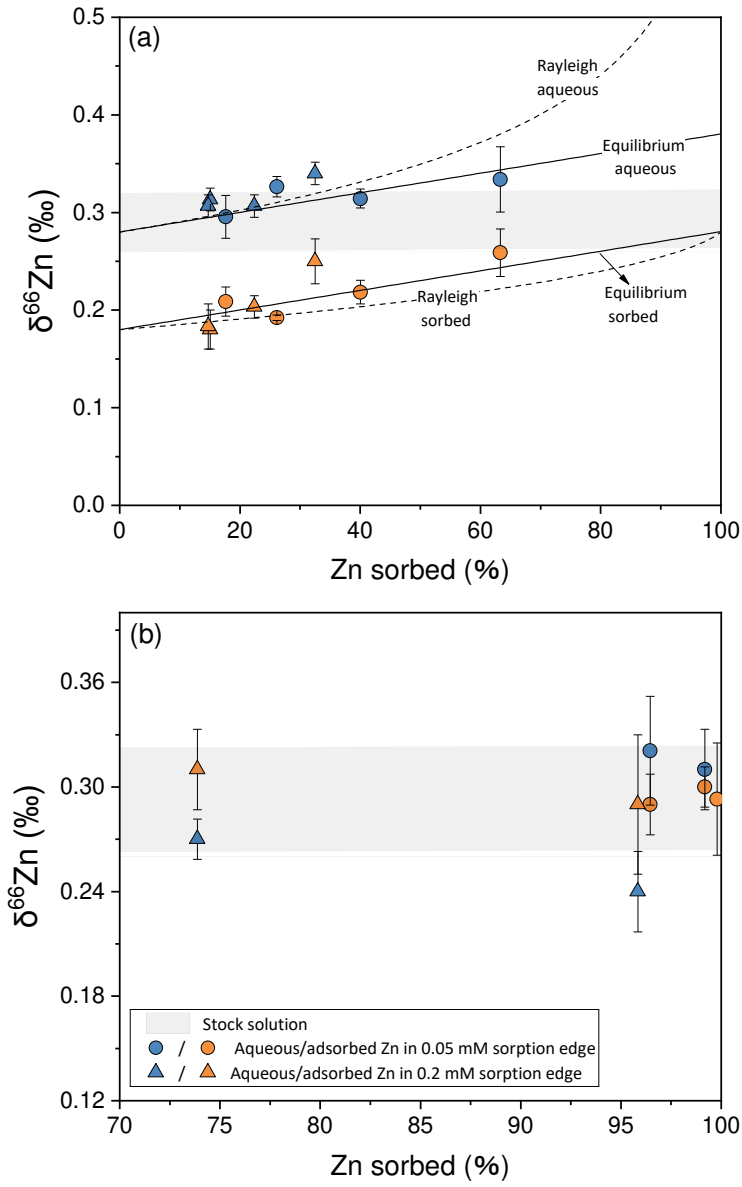

Fig. 7. Plots of Zn isotope compositions of adsorbed Zn and aqueous Zn as a function of the fraction of adsorbed Zn in experiments performed at pH values of 3.0−6.0 and Zn concentrations of 0.05−0.02 mM (a) and in experiments performed at pH values of 7.0−8.0 and Zn concentrations of 0.05−0.02 mM (b). The solid and dashed lines in figure (a) represent δ^{66}Zn values for adsorbed Zn and aqueous Zn in the batch equilibrium model and the Rayleigh fractionation model, respectively. An isotopic fractionation factor, $\alpha_{adsorbed\text{-}aqueous}$, of 0.9999 is obtained based on the best-fit batch equilibrium model. The gray shaded area indicates the initial Zn isotope composition of the stock solution used in all experiments. Error bars represent 2SD of three replicate analyses of each sample.

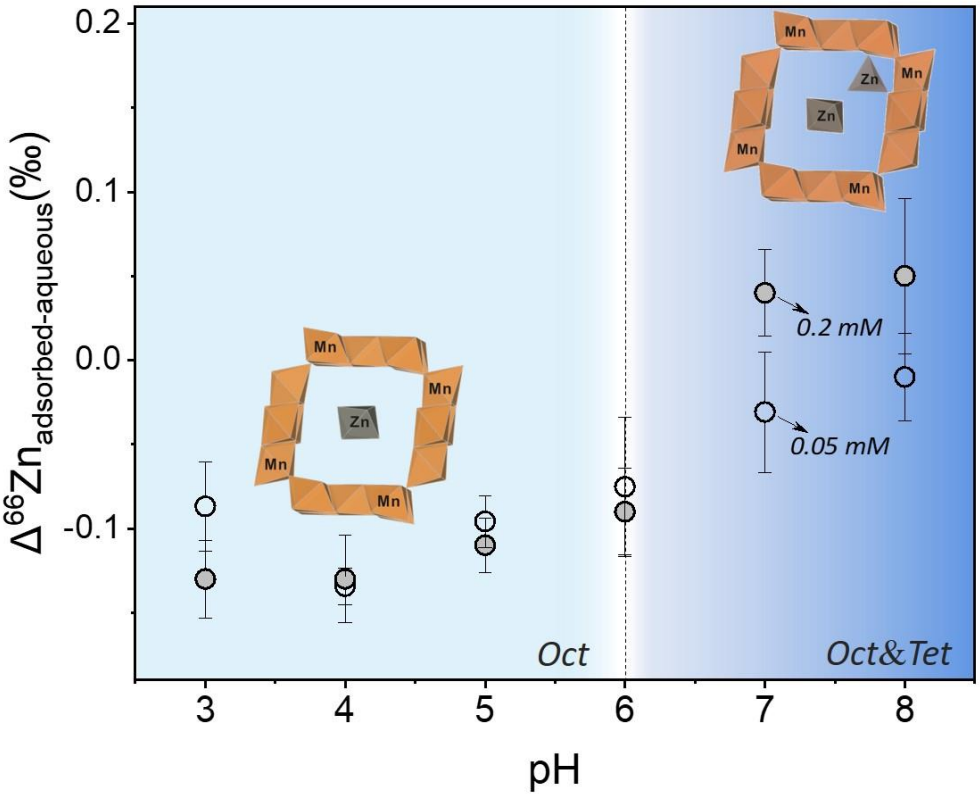

Fig. 8 Schematic diagram of the speciation of adsorbed Zn and associated isotopic fractionation on todorokite with respect to different pH values. The dashed line and shaded area are assigned based on approximate locations obtained from Zn isotope and EXAFS spectroscopic analyses. Oct refers to surface complexes of Zn coordinated with six oxygen atoms, and Tet refers to inner-sphere corner-sharing Zn complexes in tetrahedral coordination with four oxygen atoms.

Table 1. Summary of Zn isotope fractionation during adsorption onto typical environmental minerals

Minerals	pH	I (M)	Surface coverage Γ(μmol m^{-2})	$\alpha_{adsorbed-aqueous}$	$\Delta^{66}Zn_{adorbed-aqueous}$ (‰)	Reference
Goethite	5.28-6.14	0.01	*0.02- 0.03*	nd	-0.20±0.03	Pokrovsky et al., 2005
	4-8	0.1	*0.01-1.30*	1.00029	~ 0.29	Juillot et al., 2008
Hematite	5.50-6.61	0.01	*0.02-0.07*	nd	0.04 to 0.61	Pokrovsky et al., 2005
Ferrihydrite	4-8	0.1	*0.17-3.21*	1.00053	~ 0.53	Juillot et al., 2008
Birnessite	4.10-5.65	0.01	*0.03-0.08*	nd	-0.17±0.06	Pokrovsky et al., 2005
	~8.2	0	> 0.185	nd	0.05±0.08	Bryan et al., 2015
	~8.2	0.7 g/kg (synthetic seawater)	nd	nd	0.16-2.7	
Pyrolusite	6.06-8.34	0.01	*0.58-3.95*	nd	0.10±0.03	Pokrovsky et al., 2005
Calcite	8.2-8.4	0	nd	nd	0.41±0.18	Dong and Wasylenki, 2016
	8.2-8.4	0.7 g/kg (synthetic seawater)	nd	nd	0.73±0.08	
Kaolinite	<5	0.01	0.13-0.46	1.00018	0.18±0.06	Guinoiseau et al., 2016
	>5	0.1	0.02-0.47	1.00049	0.49±0.06	
Corundum	6.87-7.55	0.01	*0.22-0.51*	nd	0.10±0.09	Pokrovsky et al., 2005
Gibbsite	6.37-6.98	0.01	*0.37-0.67*	nd	0.13±0.12	Pokrovsky et al., 2005
γ-Al_2O_3	6.0-7.5	0.1	< 0.8	nd	0.02±0.07	Gou et al., 2018
	6.5-8.0	0.1	1.5-3.2	1.00047	0.47±0.03	
Quartz	5.28-5.91	0.004	< 0.6	nd	-0.01±0.06	Nelson et al., 2018
	6.53-7.15	0.1	0.6-1.4	nd	0.60±0.11	
Amorphous silica	6.23-6.99	0.004-0.100	< 1.4	nd	0.94±0.11	Nelson et al., 2018

Note. Italic surface loading values were calculated based on the data reported in related references. All uncertainties are reported using 2 sd. nd

means there are not specific descriptions in references.

Table 2. Chemical and isotopic results of zinc adsorption experiments in this study

Experiments	Time (h)	$[Zn]_{initial}$ (mM)	Adsorbed Zn(%)	Coverage (μmol m^{-2})	Zn/Mn (mol:mol)	pH	$\delta^{66}Zn_{aqueous}$	2sd	$\delta^{66}Zn_{adsorbed}$	2sd	$\Delta^{66}Zn_{adsorbed-aqueous}$	2sd	Mass balance
Todorokite adsorption kinetics	0.5	0.05	30.0	0.18	0.004	6	0.38	0.06	0.23	0.05	-0.15	0.08	0.05
	1	0.05	33.4	0.20	0.005	6	0.37	0.08	0.21	0.01	-0.16	0.08	0.04
	2	0.05	33.8	0.20	0.005	6	0.35	0.01	0.24	0.04	-0.11	0.04	0.04
	4	0.05	47.2	0.28	0.006	6	0.36	0.03	0.25	0.02	-0.11	0.04	0.03
	6	0.05	34.6	0.21	0.005	6	0.33	0.03	0.29	0.01	-0.04	0.03	0.04
	12	0.05	46.2	0.28	0.006	6	0.28	0.04	0.22	0.02	-0.06	0.04	-0.03
	24	0.05	52.1	0.30	0.007	6	0.33	0.03	0.26	0.04	-0.07	0.05	0.01
	48	0.05	55.3	0.32	0.007	6	0.34	0.02	0.25	0.01	-0.09	0.02	0.01
	120	0.05	45.7	0.29	0.006	6	0.35	0.03	0.26	0.02	-0.09	0.04	0.03
0.05 mM Todorokite adsorption edges	48	0.05	17.6	0.11	0.002	3	0.30	0.02	0.21	0.04	-0.09	0.03	0.00
	48	0.05	26.1	0.16	0.003	4	0.33	0.01	0.19	0.01	-0.13	0.01	0.01
	48	0.05	40.1	0.24	0.005	5	0.31	0.01	0.22	0.00	-0.10	0.02	0.00
	48	0.05	63.3	0.38	0.008	6	0.33	0.03	0.26	0.01	-0.08	0.04	0.01
	48	0.05	96.5	0.58	0.013	7	0.32	0.03	0.29	0.02	-0.03	0.04	0.01
	48	0.05	99.2	0.59	0.014	8	0.31	0.02	0.30	0.02	-0.01	0.03	0.02
	48	0.05	100	0.60	0.014	9			0.29	0.01			
0.2 mM Todorokite adsorption edges	48	0.2	15.1	0.36	0.008	3	0.31	0.01	0.18	0.02	-0.13	0.02	-0.01
	48	0.2	14.7	0.35	0.008	4	0.31	0.01	0.18	0.02	-0.13	0.03	-0.01
	48	0.2	22.4	0.54	0.012	5	0.31	0.01	0.20	0.01	-0.11	0.02	-0.01
	48	0.2	32.5	0.78	0.018	6	0.34	0.01	0.25	0.02	-0.09	0.03	-0.03
	48	0.2	73.9	1.77	0.040	7	0.27	0.01	0.31	0.02	0.04	0.03	-0.02
	48	0.2	95.8	2.29	0.052	8	0.24	0.02	0.29	0.04	0.05	0.05	-0.01

Note. Todorokite suspension was 0.4 g/L. The ionic strength is 0.1 $^{66}Zn_{stock}$ is 0.28 ± 0.06‰ (2SD, n = 6). Each sample is an average of three measurements on a Neptune with the 2 sd values reported to reflect internal precision on replicate. Mass balance offset = ($\delta^{66}Zn_{aqueous}$ (1-adsorbed %) +$\delta^{66}Zn_{adsorbed}$ adsorbed %)- $\delta^{66}Zn_{stock}$.

Table 3. Fitting Results of the EXAFS Spectrum for Model Compounds and Adsorption Samples ($^{c}S_0^2$ = 0.97)

Samples	Shell no.	Path	CN	R (Å)	σ^2(Å^2)	R-factor	ΔE_0 (eV)
Zinc hydroxide	1	Zn–O	3.7	1.98	0.006	0.0009	5.16
	2	Zn–Zn	10.4	3.23	0.009		
	3	Zn–Zn	3.8	4.62	0.004		
hydrozincite	1	Zn–O	4.5	1.98	0.009	0.0082	-5.98
	2	Zn–Zn	1.4	3.12	0.012		
	2	Zn–Zn	2.2	3.52	0.006		
$Zn(NO_3)_{2\ aq}$	1	Zn–O	6[a]	2.06	0.009	0.0001	2.91
Tod pH 3_0.05	1	Zn–O	6.2	2.06	0.010	0.0010	-1.28
Tod pH 3_0.2	1	Zn–O	5.8	2.06	0.009	0.0011	-1.86
Tod pH 6_0.05	1	Zn–O	5.5	2.05	0.011	0.003	-0.08
	2	Zn–Mn	3.0	3.14	0.016		
Tod pH 6_0.2	1	Zn–O	5.4	2.04	0.011	0.002	-0.70
	2	Zn–Mn	2.7	3.13	0.013		
Tod pH 8_0.05	1	Zn–O	4.8	2.01	0.009	0.0009	-4.61
	2	Zn–Mn	1.5	3.10	0.007		
Tod pH 8_0.2	1	Zn–O	5.3	2.00	0.013	0.0013	-3.16
	2	Zn–Mn	1.9	3.12	0.018		

Sample name of Tod pH 3_0.2 means Zn surface speciation on todorokite at pH 3 and initial Zn concentration of 0.2 mM. [a]Fixed value; [b]Value fixed identical to the first subshell; $^{c}S_0^2$ is the amplitude reduction factor, estimated by the fitting for $Zn(NO_3)_{2\ aq}$, and set to 0.97 for all samples; CN is the coordination number; R is the interatomic distance in Å; σ^2 in Å^2 is the Debye−Waller factor in Å^2; ΔE_0 is the energy shift in eV; R-factor is the absolute misfit between experimental data and theory.

Table 4. DFT-calculated bond distances and $10^3 \ln\beta$ $^{66}Zn/^{64}Zn$ at 300 K of geometry-optimized aqueous Zn^{2+} clusters and Zn-todorokite adsorption models.

model	$Zn^{2+}\cdot 18(H_2O)$	$Zn^{2+}\cdot 6(H_2O)$	$ZnMn_{12}O_{24}\cdot 8H_2O$		$Zn_2Mn_{12}O_{24}\cdot 8H_2O$			
			model 1	model 2	model 3		model 4	
position	–	–	center	corner	center	corner	corner	corner
d(Zn-O) (Å)	2.07	2.12	2.02	1.92	2.03	1.94	1.93	1.93
	2.08	2.12	2.05	1.92	2.07	2.07	1.94	1.97
	2.13	2.12	2.11	1.98	2.08	2.12	1.97	2.01
	2.13	2.12	2.11	2.04	2.15	2.19	1.99	2.03
	2.28	2.12	2.14	–	2.21	2.31	–	–
	2.31	2.12	2.14	–	2.27	2.39	–	–
	<2.17>	<2.12>	<2.09>	<1.96>	<2.14>	<2.17>	<1.96>	<1.98>
$10^3 \ln\beta$ (‰)	2.8	3.0	3.33	3.80	2.85	2.78	3.90	3.47

Values in angle brackets are the average distances.

Supplementary information

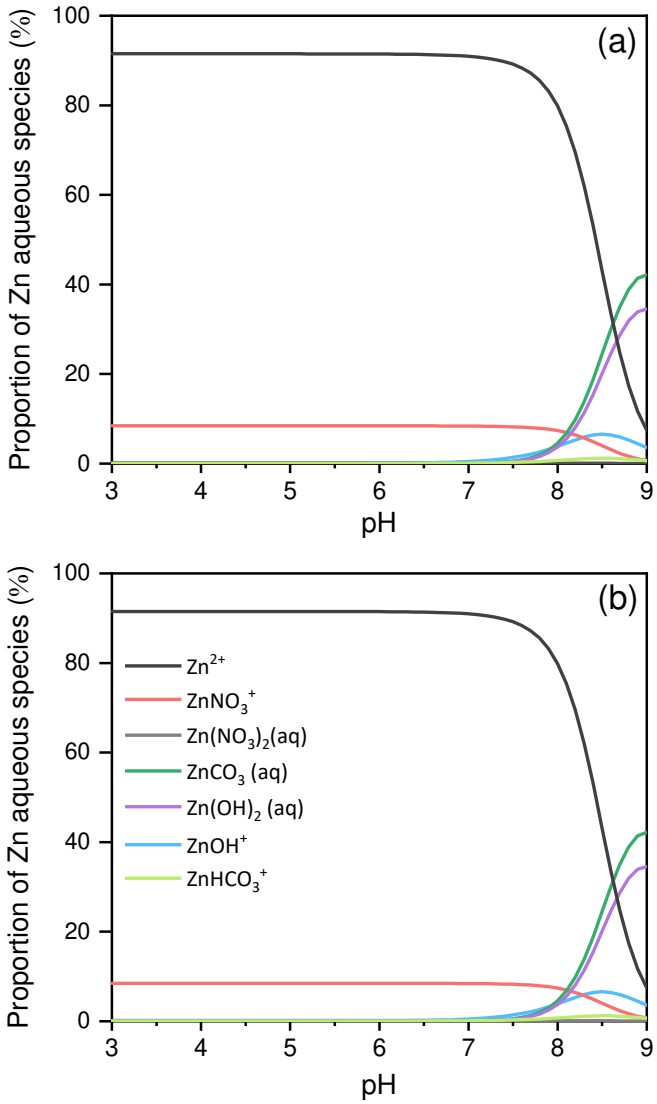

Figure S1. Zn speciation was calculated by Visual MINTEQ 3.1 as a function of pH for 0.05 mM $Zn(NO_3)_2$ (a) and 0.2 mM $Zn(NO_3)_2$ (b). The background electrolyte of 0.1 M $NaNO_3$ is used.

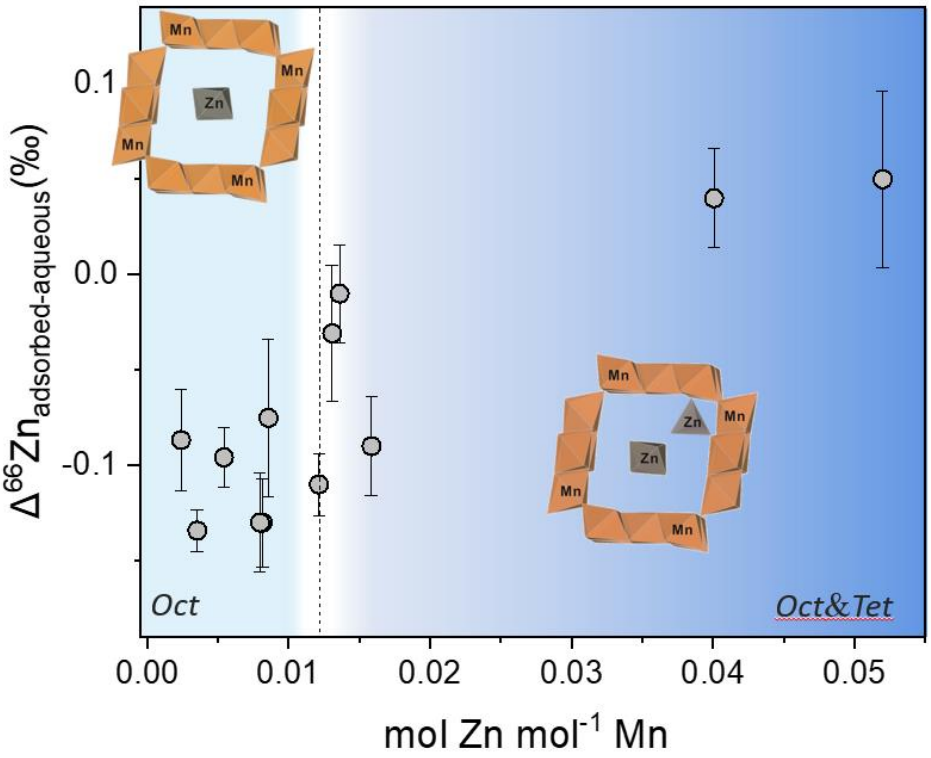

Fig. S2. Schematic diagram of the speciation of adsorbed Zn and associated isotopic fractionation on todorokite with respect to different Zn/Mn atomic ratios. The dashed line and shaded area are assigned based on approximate locations obtained from Zn isotope and EXAFS spectroscopic analyses. Oct refers to surface complexes of Zn coordinated with six oxygen atoms, and Tet refers to inner-sphere corner-sharing Zn complexes in tetrahedral coordination with four oxygen atoms.

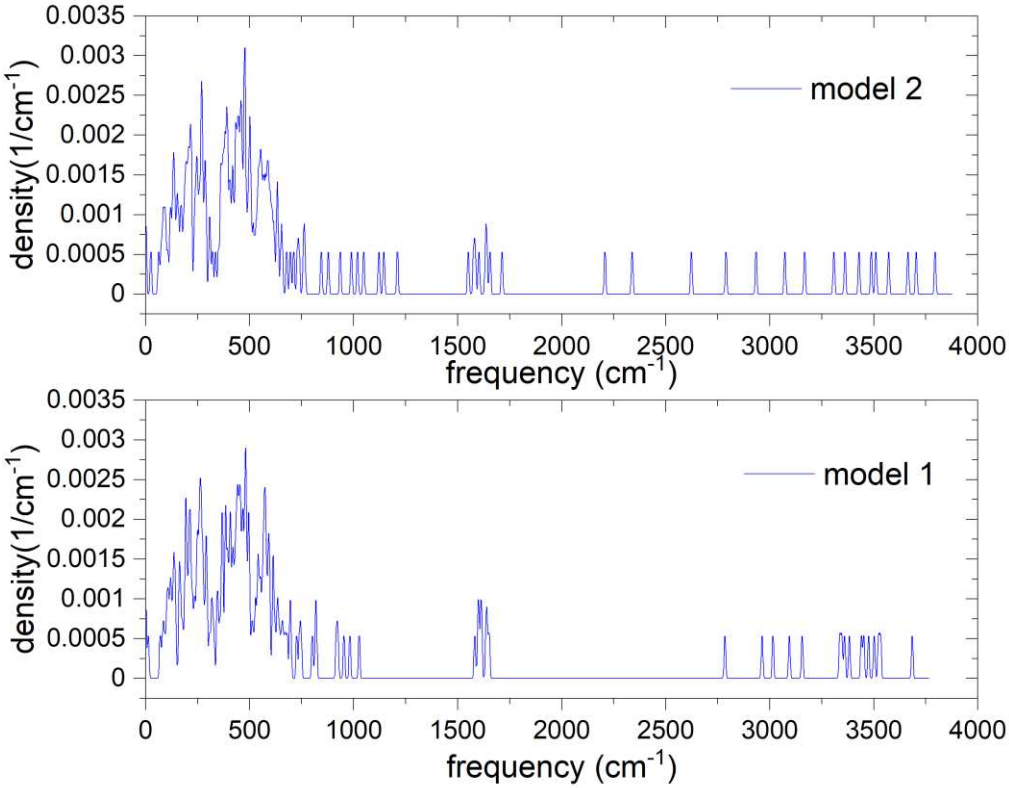

Fig. S3. Calculated vibrational frequency distribution for todorokite with octahedral Zn complex (model 1) and tetrahedral Zn complex (model 2) in the tunnel (see Table 4; Fig. 6).

mode	frequency	mode	frequency	mode	frequency	mode	frequency	mode	frequency	mode	frequency
1	-0.063994	31	166.021714	61	389.267016	91	722.102712	121	1600.290088	151	3603.178472
2	-0.053651	32	174.522895	62	394.462786	92	734.478207	122	1604.379479	152	3730.175376
3	-0.035946	33	179.861923	63	399.932967	93	756.731442	123	1617.371621	153	3757.964777
4	54.046687	34	182.908279	64	415.769212	94	765.864994	124	1631.256126	154	3783.267821
5	69.797570	35	194.011509	65	419.661500	95	784.764501	125	1635.803142	155	3788.071655
6	78.993112	36	197.309681	66	434.158955	96	801.699106	126	1646.224439	156	3788.574558
7	86.487339	37	204.988166	67	445.213720	97	828.270354	127	1656.653680	157	3802.381993
8	97.031409	38	210.381849	68	462.738553	98	847.600924	128	1662.063232	158	3807.501854
9	97.390051	39	213.763057	69	464.180890	99	856.334263	129	1676.376898	159	3808.012953
10	102.550787	40	224.425616	70	468.179548	100	878.154549	130	2928.170043	160	3822.440595
11	102.874733	41	230.050622	71	475.404656	101	884.813513	131	3031.230875	161	3825.380287
12	109.914249	42	236.135761	72	482.847085	102	904.963291	132	3036.076586	162	3827.541174
13	111.763895	43	253.763173	73	484.457018	103	922.440093	133	3068.348404	163	3828.762801
14	114.372725	44	255.139537	74	491.859407	104	927.756921	134	3111.321918	164	3834.596816
15	119.066005	45	258.509348	75	497.134984	105	962.652455	135	3161.667959	165	3855.980483
16	120.929323	46	268.911889	76	499.677391	106	975.366068	136	3224.863060		
17	124.418906	47	275.481480	77	512.831368	107	978.034905	137	3235.519503		
18	126.292720	48	276.919269	78	521.755825	108	1022.119072	138	3261.452794		
19	130.273929	49	284.757014	79	538.742739	109	1023.475738	139	3317.950758		
20	131.946246	50	290.452096	80	547.683967	110	1053.490639	140	3327.957290		
21	137.870369	51	293.524121	81	554.792466	111	1093.525621	141	3363.189707		
22	139.257778	52	312.262238	82	558.279331	112	1558.643755	142	3391.929227		
23	141.419605	53	325.094361	83	574.624535	113	1562.651430	143	3399.484043		
24	142.044549	54	331.011978	84	597.877899	114	1568.702901	144	3415.153964		
25	147.596160	55	336.721561	85	608.153959	115	1571.719201	145	3456.906280		
26	149.519126	56	350.872407	86	619.625586	116	1573.258393	146	3462.316505		
27	151.763994	57	368.459135	87	639.380829	117	1590.311060	147	3484.040549		
28	156.097570	58	370.172946	88	657.830940	118	1592.337638	148	3492.490737		
29	159.826666	59	377.709630	89	696.188202	119	1594.411632	149	3567.815999		
30	162.598666	60	380.678281	90	711.504624	120	1598.565532	150	3575.801221		

Fig. S4. Calculated vibrational frequencies of $Zn^{2+}\cdot 18(H_2O)$ in a 30 × 30 × 30 Å cell.

Table S1. Atomic coordinates (in CIF format) of geometry-optimized structures

```
#======================================================================
# Aqua_Zn_generated by Kideok Kwon
#----------------------------------------------------------------------

data_VESTA_phase_1

_chemical_name_common                  ''
_cell_length_a                         30.00000
_cell_length_b                         30.00000
_cell_length_c                         30.00000
_cell_angle_alpha                      90
_cell_angle_beta                       90
_cell_angle_gamma                      90
_space_group_name_H-M_alt              'P 1'
_space_group_IT_number                 1

loop_
_space_group_symop_operation_xyz
   'x, y, z'

loop_
   _atom_site_label
   _atom_site_occupancy
   _atom_site_fract_x
   _atom_site_fract_y
   _atom_site_fract_z
   _atom_site_adp_type
   _atom_site_U_iso_or_equiv
   _atom_site_type_symbol
   H1      1.0   0.373995   0.647149   0.451344   Uiso 0.010000 H
   H2      1.0   0.375172   0.594671   0.446471   Uiso 0.010000 H
   H3      1.0   0.664050   0.647650   0.552901   Uiso 0.010000 H
   H4      1.0   0.651402   0.690576   0.526740   Uiso 0.010000 H
   H5      1.0   0.558167   0.637646   0.445479   Uiso 0.010000 H
   H6      1.0   0.527050   0.677275   0.428415   Uiso 0.010000 H
   H7      1.0   0.625090   0.602347   0.447150   Uiso 0.010000 H
   H8      1.0   0.618912   0.628871   0.492411   Uiso 0.010000 H
   H9      1.0   0.507973   0.607608   0.391773   Uiso 0.010000 H
   H10     1.0   0.504458   0.576935   0.348737   Uiso 0.010000 H
   H11     1.0   0.354094   0.521014   0.412243   Uiso 0.010000 H
   H12     1.0   0.406154   0.526773   0.423296   Uiso 0.010000 H
   H13     1.0   0.349501   0.575706   0.597548   Uiso 0.010000 H
   H14     1.0   0.390836   0.545375   0.610490   Uiso 0.010000 H
   H15     1.0   0.401863   0.468970   0.539260   Uiso 0.010000 H
   H16     1.0   0.393092   0.418151   0.553423   Uiso 0.010000 H
   H17     1.0   0.598183   0.442423   0.534869   Uiso 0.010000 H
   H18     1.0   0.582986   0.469730   0.576217   Uiso 0.010000 H
   H19     1.0   0.496992   0.433288   0.452051   Uiso 0.010000 H
   H2O     1.0   0.490770   0.416002   0.402561   Uiso 0.010000 H
   H21     1.0   0.426994   0.614146   0.598370   Uiso 0.010000 H
   H22     1.0   0.464543   0.650542   0.593967   Uiso 0.010000 H
   H23     1.0   0.433561   0.491699   0.656905   Uiso 0.010000 H
   H24     1.0   0.420664   0.472512   0.609211   Uiso 0.010000 H
   H25     1.0   0.568377   0.563767   0.484771   Uiso 0.010000 H
   H26     1.0   0.565631   0.516469   0.508776   Uiso 0.010000 H
   H27     1.0   0.488913   0.620276   0.471052   Uiso 0.010000 H
   H28     1.0   0.436863   0.611814   0.480478   Uiso 0.010000 H
   H29     1.0   0.518362   0.457058   0.527602   Uiso 0.010000 H
   H30     1.0   0.465597   0.448004   0.529632   Uiso 0.010000 H
   H31     1.0   0.477170   0.543382   0.411290   Uiso 0.010000 H
   H32     1.0   0.476492   0.490510   0.423963   Uiso 0.010000 H
   H33     1.0   0.482223   0.576070   0.578451   Uiso 0.010000 H
   H34     1.0   0.472560   0.525762   0.589638   Uiso 0.010000 H
   H35     1.0   0.387268   0.525724   0.487917   Uiso 0.010000 H
   H36     1.0   0.392819   0.542804   0.538905   Uiso 0.010000 H
   O1      1.0   0.384749   0.619936   0.465362   Uiso 0.010000 O
```

O2	1.0	0.642630	0.659667	0.531629	Uiso 0.010000 O
O3	1.0	0.527811	0.645258	0.433840	Uiso 0.010000 O
O4	1.0	0.602671	0.610963	0.469072	Uiso 0.010000 O
O5	1.0	0.491579	0.582465	0.377989	Uiso 0.010000 O
O6	1.0	0.375234	0.535274	0.432350	Uiso 0.010000 O
O7	1.0	0.380237	0.568761	0.589555	Uiso 0.010000 O
O8	1.0	0.413511	0.443174	0.556999	Uiso 0.010000 O
O9	1.0	0.576554	0.464658	0.544731	Uiso 0.010000 O
O10	1.0	0.499681	0.441578	0.420460	Uiso 0.010000 O
O11	1.0	0.459077	0.619708	0.602454	Uiso 0.010000 O
O12	1.0	0.428823	0.499963	0.625838	Uiso 0.010000 O
O13	1.0	0.467933	0.603201	0.490181	Uiso 0.010000 O
O14	1.0	0.549529	0.536836	0.488700	Uiso 0.010000 O
O15	1.0	0.489945	0.461273	0.511344	Uiso 0.010000 O
O16	1.0	0.463951	0.520599	0.432700	Uiso 0.010000 O
O17	1.0	0.489360	0.544616	0.568381	Uiso 0.010000 O
O18	1.0	0.405199	0.522080	0.515766	Uiso 0.010000 O
Zn1	1.0	0.479362	0.535865	0.500399	Uiso 0.010000 Zn

```
#======================================================================
# todorokite with center Zn + corner Zn generated by Kideok Kwon
#----------------------------------------------------------------------

data_VESTA_phase_1

_chemical_name_common                    ''
_cell_length_a                           10.09752
_cell_length_b                           5.76478
_cell_length_c                           9.67134
_cell_angle_alpha                        90
_cell_angle_beta                         95.56499
_cell_angle_gamma                        90
_space_group_name_H-M_alt                'P 1'
_space_group_IT_number                   1

loop_
_space_group_symop_operation_xyz
   'x, y, z'

loop_
   _atom_site_label
   _atom_site_occupancy
   _atom_site_fract_x
   _atom_site_fract_y
   _atom_site_fract_z
   _atom_site_adp_type
   _atom_site_U_iso_or_equiv
   _atom_site_type_symbol
   H1      1.0   0.329082   0.335333   0.746587   Uiso 0.010000 H
   H2      1.0   0.329039   0.584329   0.669824   Uiso 0.010000 H
   H3      1.0   0.692644   0.400854   0.345317   Uiso 0.010000 H
   H4      1.0   0.543313   0.468731   0.258119   Uiso 0.010000 H
   H5      1.0   0.261840   0.570551   0.388263   Uiso 0.010000 H
   H6      1.0   0.369294   0.776457   0.398045   Uiso 0.010000 H
   H7      1.0   0.709554   0.105743   0.640013   Uiso 0.010000 H
   H8      1.0   0.581035   0.056236   0.717826   Uiso 0.010000 H
   H9      1.0   0.275043   0.103937   0.378869   Uiso 0.010000 H
   H10     1.0   0.407806   0.078529   0.300580   Uiso 0.010000 H
   H11     1.0   0.702185   0.565439   0.646803   Uiso 0.010000 H
   H12     1.0   0.583073   0.570155   0.744982   Uiso 0.010000 H
   H13     1.0   0.373726   0.940398   0.589971   Uiso 0.010000 H
   H14     1.0   0.400259   0.918803   0.752904   Uiso 0.010000 H
   H15     1.0   0.617226   0.723049   0.385099   Uiso 0.010000 H
   H16     1.0   0.618008   0.952325   0.485416   Uiso 0.010000 H
   O1      1.0   0.448240   0.014121   0.127484   Uiso 0.010000 O
   O2      1.0   0.917209   0.011561   0.157400   Uiso 0.010000 O
   O3      1.0   0.873600   0.016294   0.651025   Uiso 0.010000 O
   O4      1.0   0.543243   0.006960   0.891854   Uiso 0.010000 O
   O5      1.0   0.058278   0.013046   0.848859   Uiso 0.010000 O
   O6      1.0   0.103412   0.016556   0.353576   Uiso 0.010000 O
   O7      1.0   0.145371   0.258689   0.113393   Uiso 0.010000 O
   O8      1.0   0.685263   0.245323   0.092979   Uiso 0.010000 O
   O9      1.0   0.892520   0.257577   0.390115   Uiso 0.010000 O
   O10     1.0   0.833373   0.266525   0.888525   Uiso 0.010000 O
   O11     1.0   0.312773   0.264223   0.930396   Uiso 0.010000 O
   O12     1.0   0.069519   0.264906   0.601388   Uiso 0.010000 O
   O13     1.0   0.459285   0.504169   0.131681   Uiso 0.010000 O
   O14     1.0   0.925808   0.512994   0.150302   Uiso 0.010000 O
   O15     1.0   0.872516   0.513463   0.649873   Uiso 0.010000 O
   O16     1.0   0.556568   0.512140   0.903845   Uiso 0.010000 O
   O17     1.0   0.059255   0.513687   0.847900   Uiso 0.010000 O
   O18     1.0   0.100569   0.511510   0.354063   Uiso 0.010000 O
   O19     1.0   0.145738   0.763389   0.113709   Uiso 0.010000 O
   O20     1.0   0.686095   0.769120   0.091608   Uiso 0.010000 O
   O21     1.0   0.898750   0.767196   0.390571   Uiso 0.010000 O
   O22     1.0   0.834210   0.756755   0.888264   Uiso 0.010000 O
   O23     1.0   0.314019   0.755205   0.937976   Uiso 0.010000 O
   O24     1.0   0.069562   0.760764   0.601342   Uiso 0.010000 O
```

O25	1.0	0.338194	0.411334	0.656275	Uiso 0.010000 O
O26	1.0	0.601737	0.452289	0.356979	Uiso 0.010000 O
O27	1.0	0.359014	0.606472	0.399259	Uiso 0.010000 O
O28	1.0	0.609656	0.109317	0.626360	Uiso 0.010000 O
O29	1.0	0.374168	0.096745	0.394720	Uiso 0.010000 O
O30	1.0	0.605579	0.600938	0.646554	Uiso 0.010000 O
O31	1.0	0.339709	0.871634	0.671660	Uiso 0.010000 O
O32	1.0	0.622136	0.898502	0.387306	Uiso 0.010000 O
Mn1	1.0	0.496473	0.257776	0.011920	Uiso 0.010000 Mn
Mn2	1.0	-0.012346	0.013582	0.501206	Uiso 0.010000 Mn
Mn3	1.0	0.496738	0.758511	0.016606	Uiso 0.010000 Mn
Mn4	1.0	-0.017667	0.513531	0.500538	Uiso 0.010000 Mn
Mn5	1.0	0.215415	0.510814	1.011237	Uiso 0.010000 Mn
Mn6	1.0	0.019128	0.760034	0.238736	Uiso 0.010000 Mn
Mn7	1.0	0.769427	0.510264	-0.000620	Uiso 0.010000 Mn
Mn8	1.0	0.965490	0.762936	0.763229	Uiso 0.010000 Mn
Mn9	1.0	0.219340	0.010009	1.011192	Uiso 0.010000 Mn
Mn10	1.0	0.017318	0.264693	0.238158	Uiso 0.010000 Mn
Mn11	1.0	0.759733	0.010306	-0.024409	Uiso 0.010000 Mn
Mn12	1.0	0.966294	0.263709	0.763158	Uiso 0.010000 Mn
Zn1	1.0	0.746451	0.996133	0.258490	Uiso 0.010000 Zn
Zn2	1.0	0.480904	0.382990	0.523201	Uiso 0.010000 Zn

```
#======================================================================
# todorokite with center Zn generated by Kideok Kwon
#----------------------------------------------------------------------

data_VESTA_phase_1

_chemical_name_common                    ''
_cell_length_a                           10.00397
_cell_length_b                           5.76920
_cell_length_c                           9.67044
_cell_angle_alpha                        90
_cell_angle_beta                         94.26335
_cell_angle_gamma                        90
_space_group_name_H-M_alt                'P 1'
_space_group_IT_number                   1

loop_
_space_group_symop_operation_xyz
   'x, y, z'

loop_
   _atom_site_label
   _atom_site_occupancy
   _atom_site_fract_x
   _atom_site_fract_y
   _atom_site_fract_z
   _atom_site_adp_type
   _atom_site_U_iso_or_equiv
   _atom_site_type_symbol
   H1      1.0   0.341869   0.262644   0.752013   Uiso 0.010000 H
   H2      1.0   0.328182   0.482901   0.658062   Uiso 0.010000 H
   H3      1.0   0.636490   0.501912   0.382005   Uiso 0.010000 H
   H4      1.0   0.643517   0.261186   0.299327   Uiso 0.010000 H
   H5      1.0   0.272456   0.543852   0.388503   Uiso 0.010000 H
   H6      1.0   0.402208   0.698244   0.392557   Uiso 0.010000 H
   H7      1.0   0.596428   0.019193   0.717616   Uiso 0.010000 H
   H8      1.0   0.472684  -0.115748   0.641457   Uiso 0.010000 H
   H9      1.0   0.277399   0.057560   0.369550   Uiso 0.010000 H
   H10     1.0   0.410352   0.049998   0.287362   Uiso 0.010000 H
   H11     1.0   0.705206   0.505730   0.640341   Uiso 0.010000 H
   H12     1.0   0.593612   0.512594   0.748463   Uiso 0.010000 H
   H13     1.0   0.244164   0.814774   0.634418   Uiso 0.010000 H
   H14     1.0   0.329095   0.791888   0.778320   Uiso 0.010000 H
   H15     1.0   0.624653   0.834625   0.487160   Uiso 0.010000 H
   H16     1.0   0.727492   0.818948   0.372211   Uiso 0.010000 H
   O1      1.0   0.458837   0.073289   0.131959   Uiso 0.010000 O
   O2      1.0   0.924666   0.073811   0.144040   Uiso 0.010000 O
   O3      1.0   0.878288   0.074464   0.658964   Uiso 0.010000 O
   O4      1.0   0.589726   0.071542   0.916688   Uiso 0.010000 O
   O5      1.0   0.064936   0.073457   0.850459   Uiso 0.010000 O
   O6      1.0   0.100884   0.074849   0.345843   Uiso 0.010000 O
   O7      1.0   0.151020   0.322984   0.111674   Uiso 0.010000 O
   O8      1.0   0.694840   0.321775   0.109038   Uiso 0.010000 O
   O9      1.0   0.903566   0.325263   0.395243   Uiso 0.010000 O
   O10     1.0   0.838023   0.323876   0.905146   Uiso 0.010000 O
   O11     1.0   0.328633   0.319560   0.935086   Uiso 0.010000 O
   O12     1.0   0.071244   0.326480   0.602968   Uiso 0.010000 O
   O13     1.0   0.455824   0.571511   0.127981   Uiso 0.010000 O
   O14     1.0   0.924251   0.574208   0.144290   Uiso 0.010000 O
   O15     1.0   0.877164   0.574746   0.658008   Uiso 0.010000 O
   O16     1.0   0.588620   0.572929   0.918092   Uiso 0.010000 O
   O17     1.0   0.064715   0.574973   0.850285   Uiso 0.010000 O
   O18     1.0   0.099898   0.574428   0.346235   Uiso 0.010000 O
   O19     1.0   0.151339   0.822945   0.112247   Uiso 0.010000 O
   O20     1.0   0.696500   0.822864   0.108673   Uiso 0.010000 O
   O21     1.0   0.902485   0.826741   0.394743   Uiso 0.010000 O
   O22     1.0   0.837438   0.822673   0.904065   Uiso 0.010000 O
   O23     1.0   0.329180   0.823735   0.938196   Uiso 0.010000 O
   O24     1.0   0.073996   0.825933   0.602535   Uiso 0.010000 O
```

O25	1.0	0.338389	0.309438	0.653753	Uiso 0.010000 O
O26	1.0	0.632438	0.325916	0.391194	Uiso 0.010000 O
O27	1.0	0.370678	0.539251	0.408232	Uiso 0.010000 O
O28	1.0	0.556589	-0.025041	0.625059	Uiso 0.010000 O
O29	1.0	0.375376	0.027752	0.381467	Uiso 0.010000 O
O30	1.0	0.609388	0.474459	0.651008	Uiso 0.010000 O
O31	1.0	0.333419	0.764574	0.675731	Uiso 0.010000 O
O32	1.0	0.635632	0.775128	0.392308	Uiso 0.010000 O
Mn1	1.0	0.510591	0.323515	0.025841	Uiso 0.010000 Mn
Mn2	1.0	-0.015184	0.077556	0.503059	Uiso 0.010000 Mn
Mn3	1.0	0.513070	0.821507	0.028718	Uiso 0.010000 Mn
Mn4	1.0	-0.015169	0.573386	0.501514	Uiso 0.010000 Mn
Mn5	1.0	0.227966	0.571696	1.014711	Uiso 0.010000 Mn
Mn6	1.0	0.016443	0.825107	0.236694	Uiso 0.010000 Mn
Mn7	1.0	0.770980	0.573025	0.011136	Uiso 0.010000 Mn
Mn8	1.0	0.968235	0.824988	0.768707	Uiso 0.010000 Mn
Mn9	1.0	0.224646	0.073347	1.011379	Uiso 0.010000 Mn
Mn10	1.0	0.016311	0.323868	0.237225	Uiso 0.010000 Mn
Mn11	1.0	0.769238	0.072862	0.009023	Uiso 0.010000 Mn
Mn12	1.0	0.968815	0.324214	0.768275	Uiso 0.010000 Mn
Zn1	1.0	0.482823	0.270441	0.515699	Uiso 0.010000 Zn

```
#======================================================================
# todorokite with corner Zn + corner Zn generated by Kideok Kwon
#----------------------------------------------------------------------

data_VESTA_phase_1

_chemical_name_common                    ''
_cell_length_a                           10.09522
_cell_length_b                           5.76410
_cell_length_c                           9.66638
_cell_angle_alpha                        90
_cell_angle_beta                         95.78459
_cell_angle_gamma                        90
_space_group_name_H-M_alt                'P 1'
_space_group_IT_number                   1

loop_
_space_group_symop_operation_xyz
   'x, y, z'

loop_
   _atom_site_label
   _atom_site_occupancy
   _atom_site_fract_x
   _atom_site_fract_y
   _atom_site_fract_z
   _atom_site_adp_type
   _atom_site_U_iso_or_equiv
   _atom_site_type_symbol
   H1      1.0   0.472122   0.549643   0.743744   Uiso 0.010000 H
   H2      1.0   0.392869   0.585332   0.583717   Uiso 0.010000 H
   H3      1.0   0.643034   0.436447   0.488573   Uiso 0.010000 H
   H4      1.0   0.525494   0.562986   0.382897   Uiso 0.010000 H
   H5      1.0   0.373619   0.789745   0.399354   Uiso 0.010000 H
   H6      1.0   0.288104   0.555216   0.385852   Uiso 0.010000 H
   H7      1.0   0.654600   0.143853   0.618245   Uiso 0.010000 H
   H8      1.0   0.742558   0.369640   0.658576   Uiso 0.010000 H
   H9      1.0   0.282547   0.078643   0.356923   Uiso 0.010000 H
   H10     1.0   0.419732   0.071392   0.282933   Uiso 0.010000 H
   H11     1.0   0.402547   1.063528   0.543140   Uiso 0.010000 H
   H12     1.0   0.465257   0.975639   0.693390   Uiso 0.010000 H
   H13     1.0   0.634421   0.759849   0.557645   Uiso 0.010000 H
   H14     1.0   0.698237   0.805664   0.712153   Uiso 0.010000 H
   H15     1.0   0.770179   2.164562   0.386634   Uiso 0.010000 H
   H16     1.0   0.670950   2.164832   0.252933   Uiso 0.010000 H
   O1      1.0   0.451788   0.023936   0.126654   Uiso 0.010000 O
   O2      1.0   0.936898   0.015081   0.166213   Uiso 0.010000 O
   O3      1.0   0.902779   0.017592   0.665981   Uiso 0.010000 O
   O4      1.0   0.560735   0.014624   0.905174   Uiso 0.010000 O
   O5      1.0   0.078192   0.016516   0.868787   Uiso 0.010000 O
   O6      1.0   0.119993   0.017780   0.364526   Uiso 0.010000 O
   O7      1.0   0.162585   0.268296   0.126127   Uiso 0.010000 O
   O8      1.0   0.692316   0.267142   0.093387   Uiso 0.010000 O
   O9      1.0   0.923070   0.265755   0.414999   Uiso 0.010000 O
   O10     1.0   0.850827   0.267032   0.901157   Uiso 0.010000 O
   O11     1.0   0.319691   0.265470   0.929000   Uiso 0.010000 O
   O12     1.0   0.104190   0.267199   0.625196   Uiso 0.010000 O
   O13     1.0   0.447307   0.514552   0.122253   Uiso 0.010000 O
   O14     1.0   0.934840   0.519170   0.168788   Uiso 0.010000 O
   O15     1.0   0.899778   0.515127   0.666665   Uiso 0.010000 O
   O16     1.0   0.561985   0.522528   0.903524   Uiso 0.010000 O
   O17     1.0   0.079132   0.515796   0.869181   Uiso 0.010000 O
   O18     1.0   0.120432   0.514383   0.365345   Uiso 0.010000 O
   O19     1.0   0.164630   0.767213   0.130606   Uiso 0.010000 O
   O20     1.0   0.693604   0.764295   0.100527   Uiso 0.010000 O
   O21     1.0   0.919087   0.764468   0.411156   Uiso 0.010000 O
   O22     1.0   0.846305   0.767426   0.898249   Uiso 0.010000 O
   O23     1.0   0.318708   0.769292   0.938174   Uiso 0.010000 O
   O24     1.0   0.098022   0.764104   0.621677   Uiso 0.010000 O
```

O25	1.0	0.384730	0.552922	0.685044	Uiso 0.010000 O
O26	1.0	0.625339	0.563953	0.408267	Uiso 0.010000 O
O27	1.0	0.377504	0.618066	0.419154	Uiso 0.010000 O
O28	1.0	0.654695	0.317934	0.615727	Uiso 0.010000 O
O29	1.0	0.381223	0.069576	0.375576	Uiso 0.010000 O
O30	1.0	0.382300	1.031107	0.640687	Uiso 0.010000 O
O31	1.0	0.631043	0.861531	0.639677	Uiso 0.010000 O
O32	1.0	0.687208	2.084726	0.345051	Uiso 0.010000 O
Mn1	1.0	0.508154	0.268628	0.012029	Uiso 0.010000 Mn
Mn2	1.0	0.013182	0.014300	0.519079	Uiso 0.010000 Mn
Mn3	1.0	0.502436	0.767779	0.015466	Uiso 0.010000 Mn
Mn4	1.0	0.011436	0.516878	0.517795	Uiso 0.010000 Mn
Mn5	1.0	0.238055	0.520119	1.029275	Uiso 0.010000 Mn
Mn6	1.0	0.035161	0.766765	0.250284	Uiso 0.010000 Mn
Mn7	1.0	0.778579	0.515823	0.001329	Uiso 0.010000 Mn
Mn8	1.0	0.987846	0.766110	0.779482	Uiso 0.010000 Mn
Mn9	1.0	0.233464	0.015257	1.025761	Uiso 0.010000 Mn
Mn10	1.0	0.030444	0.266515	0.251281	Uiso 0.010000 Mn
Mn11	1.0	0.777335	0.018124	0.000517	Uiso 0.010000 Mn
Mn12	1.0	0.984529	0.265758	0.783488	Uiso 0.010000 Mn
Zn1	1.0	0.735840	0.756184	0.303774	Uiso 0.010000 Zn
Zn2	1.0	0.286532	0.277322	0.725163	Uiso 0.010000 Zn

```
#======================================================================
# todorokite with corner Zn generated by Kideok Kwon
#----------------------------------------------------------------------

data_VESTA_phase_1

_chemical_name_common                    ''
_cell_length_a                           9.94486
_cell_length_b                           5.76418
_cell_length_c                           9.70154
_cell_angle_alpha                        90
_cell_angle_beta                         93.43745
_cell_angle_gamma                        90
_space_group_name_H-M_alt                'P 1'
_space_group_IT_number                   1

loop_
_space_group_symop_operation_xyz
   'x, y, z'

loop_
   _atom_site_label
   _atom_site_occupancy
   _atom_site_fract_x
   _atom_site_fract_y
   _atom_site_fract_z
   _atom_site_adp_type
   _atom_site_B_iso_or_equiv
   _atom_site_type_symbol
   H        1.0    0.304897    0.487388    0.721618    Biso 1.000000 H
   H        1.0    0.352542    0.511284    0.566401    Biso 1.000000 H
   H        1.0    0.622892    0.439881    0.513773    Biso 1.000000 H
   H        1.0    0.518967    0.525480    0.386922    Biso 1.000000 H
   H        1.0    0.287279    0.576156    0.364558    Biso 1.000000 H
   H        1.0    0.372125    0.801219    0.413990    Biso 1.000000 H
   H        1.0    0.646127   -0.249696    0.674843    Biso 1.000000 H
   H        1.0    0.504945   -0.101978    0.649735    Biso 1.000000 H
   H        1.0    0.273188    0.091565    0.371738    Biso 1.000000 H
   H        1.0    0.406961    0.074003    0.293199    Biso 1.000000 H
   H        1.0    0.641848    0.196092    0.667202    Biso 1.000000 H
   H        1.0    0.524343    0.381423    0.675452    Biso 1.000000 H
   H        1.0    0.345430    1.118394    0.658197    Biso 1.000000 H
   H        1.0    0.338452    0.904198    0.761934    Biso 1.000000 H
   H        1.0    0.628642    0.925717    0.486242    Biso 1.000000 H
   H        1.0    0.680459    0.809857    0.347989    Biso 1.000000 H
   O        1.0    0.450590    0.045569    0.126161    Biso 1.000000 O
   O        1.0    0.922135    0.040819    0.147429    Biso 1.000000 O
   O        1.0    0.884965    0.040261    0.660698    Biso 1.000000 O
   O        1.0    0.592619    0.042563    0.919584    Biso 1.000000 O
   O        1.0    0.071025    0.041175    0.848940    Biso 1.000000 O
   O        1.0    0.100825    0.042338    0.342549    Biso 1.000000 O
   O        1.0    0.151022    0.291394    0.108329    Biso 1.000000 O
   O        1.0    0.693652    0.289998    0.113106    Biso 1.000000 O
   O        1.0    0.899591    0.288321    0.396040    Biso 1.000000 O
   O        1.0    0.843246    0.291311    0.907938    Biso 1.000000 O
   O        1.0    0.329970    0.292666    0.930919    Biso 1.000000 O
   O        1.0    0.078120    0.289599    0.599697    Biso 1.000000 O
   O        1.0    0.450507    0.541467    0.125820    Biso 1.000000 O
   O        1.0    0.923265    0.540752    0.146318    Biso 1.000000 O
   O        1.0    0.885353    0.543023    0.660409    Biso 1.000000 O
   O        1.0    0.592461    0.544428    0.920322    Biso 1.000000 O
   O        1.0    0.072959    0.540905    0.847313    Biso 1.000000 O
   O        1.0    0.102034    0.538106    0.341360    Biso 1.000000 O
   O        1.0    0.150108    0.792022    0.107534    Biso 1.000000 O
   O        1.0    0.695218    0.791346    0.109611    Biso 1.000000 O
   O        1.0    0.905829    0.788243    0.398841    Biso 1.000000 O
   O        1.0    0.841690    0.790292    0.905542    Biso 1.000000 O
   O        1.0    0.331273    0.792464    0.930849    Biso 1.000000 O
   O        1.0    0.080403    0.789067    0.600381    Biso 1.000000 O
```

O	1.0	0.360898	0.416543	0.654317	Biso 1.000000 O
O	1.0	0.618098	0.491260	0.408708	Biso 1.000000 O
O	1.0	0.370323	0.624121	0.417069	Biso 1.000000 O
O	1.0	0.606294	-0.111290	0.630658	Biso 1.000000 O
O	1.0	0.371753	0.074773	0.386872	Biso 1.000000 O
O	1.0	0.621552	0.363409	0.654752	Biso 1.000000 O
O	1.0	0.358678	0.947372	0.667112	Biso 1.000000 O
O	1.0	0.643118	0.955201	0.381436	Biso 1.000000 O
Mn	1.0	0.507150	0.293803	0.021721	Biso 1.000000 Mn
Mn	1.0	-0.009262	0.037876	0.503795	Biso 1.000000 Mn
Mn	1.0	0.511816	0.791464	0.025165	Biso 1.000000 Mn
Mn	1.0	-0.009735	0.542192	0.503355	Biso 1.000000 Mn
Mn	1.0	0.229429	0.542451	1.009925	Biso 1.000000 Mn
Mn	1.0	0.017287	0.790201	0.236416	Biso 1.000000 Mn
Mn	1.0	0.771657	0.543481	0.009258	Biso 1.000000 Mn
Mn	1.0	0.976228	0.790621	0.767348	Biso 1.000000 Mn
Mn	1.0	0.227847	0.041979	1.007894	Biso 1.000000 Mn
Mn	1.0	0.018961	0.290760	0.233930	Biso 1.000000 Mn
Mn	1.0	0.770840	0.039067	0.007441	Biso 1.000000 Mn
Mn	1.0	0.974805	0.290775	0.767263	Biso 1.000000 Mn
Zn	1.0	0.706911	0.246373	0.315942	Biso 1.000000 Zn